

## High Velocity Circumstellar Gas Orbiting a White Dwarf Star

B. ZUCKERMAN <sup>1</sup>, ÉRIKA LE BOURDAIS <sup>2,3</sup>, BETH L. KLEIN <sup>1</sup>, PATRICK DUFOUR <sup>2,3</sup>, CARL MELIS <sup>4</sup>,  
ALYCIA J. WEINBERGER <sup>5</sup>, SIYI XU (许偲艺) <sup>6</sup>, ANTOINE BÉDARD <sup>7</sup> AND DETLEV KOESTER <sup>8</sup>

<sup>1</sup>*Department of Physics and Astronomy, University of California, Los Angeles, Los Angeles, CA 90095-1562, USA*

<sup>2</sup>*Trottier Institute for Research on Exoplanets and Département de physique, Université de Montréal, Ave. Thérèse-Lavoie-Roux Montréal, Québec H2V 0B3, Canada*

<sup>3</sup>*Centre de recherche en astrophysique du Québec, Montréal, Québec, Canada*

<sup>4</sup>*Department of Astronomy and Astrophysics, University of California, San Diego, La Jolla, CA 92093-0424, USA*

<sup>5</sup>*Earth and Planets Laboratory, Carnegie Institution for Science, 5241 Broad Branch Rd. NW, Washington, DC 20015, USA*

<sup>6</sup>*Gemini Observatory/NOIRLab, 950 N Cherry Ave., Tucson, AZ 85719*

<sup>7</sup>*Department of Physics, University of Warwick, Coventry, CV4 7AL, UK*

<sup>8</sup>*Institut für Theoretische Physik und Astrophysik, University of Kiel, D-24098 Kiel, Germany*

Submitted to ApJ

### ABSTRACT

Numerous white dwarf stars are known to be orbited by disks of gas and dust. To date, broad,  $\sim 300$  km s<sup>-1</sup> wide, gaseous circumstellar absorption features have only been reported for the already iconic WD 1145+017, where one is witnessing the breakup of an extrasolar asteroid in real time. We report here the discovery of absorption from circumstellar gas around a second white dwarf (WD J02340406) with similarly broad features. The observed lines are carried by ions of Ca, Cr, Fe, Ti, Mg, Mn, Na, O, Si, Sc, Sr, Ti, and V. In addition, deep, non-photospheric lines of Si IV are seen in the ultraviolet; we compare these with Si IV lines previously seen in the ultraviolet spectra of various other white dwarfs. The apparent broadband flux of WD 1145+017 is known to change often and rapidly as chunks of the asteroid pass between the star and Earth. No such variations are seen in the brightness of WD J02340406. In addition, while the strength/structure of circumstellar absorption features at WD 1145+017 has changed dramatically with time, nothing similar is seen at WD J02340406. Excess infrared emission at WD J0234-0406 indicates the presence of circumstellar dust particles.

### 1. INTRODUCTION

Optical and ultraviolet spectroscopy have revealed the presence of elements heavier than helium in the photospheres of 25% - 50% of white dwarf stars (B. Zuckerman et al. 2003, 2010; D. Koester et al. 2014). A much smaller percentage shows evidence for orbiting dust particles, and an even smaller percentage for orbiting gas. These various phenomena are now understood to be, typically, the consequences of the accretion of rocky minor planets (asteroids) by the stars (D. Veras 2016, 2021; J. Farihi 2016; M. Jura & E. D. Young 2014; B. Zuckerman & E. D. Young 2018). Sometimes the accreted body could be a Kuiper-Belt analog (S. Xu et al. 2017), a large moon (A. E. Doyle et al. 2021), or even a major planet (M. Jura et al. 2009).

Direct evidence for orbiting gas usually takes the form of emission lines from one or a variety of elements (e.g., B. T. Gänsicke et al. 2006; C. Melis et al. 2020; E. Denihy et al. 2020; N. P. Gentile Fusillo et al. 2021). These lines often display a wide range of radial velocities indicative of rapid orbital motions in a disk. Circumstellar absorption features are much rarer, in part because the orbiting material must lie in a plane that intersects the line of sight from Earth to star. For nearly circular circumstellar orbits, one would anticipate a narrow absorption line. To date, examples of a few such narrow lines have been presented in J. H. Debes et al. (2012), A. Steele et al. (2021), B. T. Gänsicke et al. (2012) and Z. P. Vanderbosch et al. (2021). When there is evidence for circumstellar dust or gas at a white dwarf, there are also absorption lines from one or more elements in the photospheric spectrum of the star. The interpretation is that the dust and gas accrete onto the star and remains

in the photosphere for a while in the form of various ions before it sinks into the interior out of sight.

White dwarf WD 1145+017 differs from those stars mentioned in the preceding paragraph in that it displays numerous absorption features, each of which covers a wide range of velocities ( $\sim 300 \text{ km s}^{-1}$ , S. Xu et al. 2016). This indicates that the orbits of the absorbing gas must have a substantial radial component. Models for how this might occur are considered in J. Budaj et al. (2022) and references therein. Substantial variations in the broadband flux of WD 1145+017 were first discovered in the analysis of Kepler K2 data by A. Vanderburg et al. (2015). These variations have been interpreted as due to the passage between the star and Earth of chunks of a disintegrating asteroid. The gaseous absorption features' strengths and radial velocities at WD 1145+017 also vary with time (S. Redfield et al. 2017; P. W. Cauley et al. 2018; S. Xu et al. 2019; M. Fortin-Archambault et al. 2020; E. Le Bourdais et al. 2024).

In this paper, we consider a second white dwarf that displays numerous broad circumstellar absorption lines from a variety of elements. The Gaia DR3 position of the white dwarf is 02 34 15.51; -04 06 09.28. The only published analysis of the spectrum of the star is by N. P. Gentile Fusillo et al. (2021, hereafter GF21), who denote it as WD J0234-0406. Here, we use the same name although the star has been previously identified in the literature as PHL 1360.

GF21 found that WD J0234-0406 has an unusually large H mass fraction compared to other He-rich white dwarfs and they measured extremely wide Ca II IR triplet profiles in emission. Quoting from their paper, “the emission profiles appear relatively symmetric that could suggest a circular disc.” They do not report any non-photospheric absorption lines. So the principal addition of the present paper is the discovery of the broad absorption features; these indicate that the orbiting disk is far from circular.

As discussed below, WD J0234-0406 and WD 1145+017 have some common features, but also some that differ. Perhaps the most striking difference is the lack of measurable secular variations in both the broadband flux and the circumstellar line characteristics from WD J0234-0406 (see Section 4.1). This suggests that the asteroid(s) that were the parent body for the observed gas and dust have already been broken into tiny pieces, well distributed in the circumstellar material.

Two unusual absorption lines seen in the ultraviolet spectrum of WD J0234-0406 arise from Si IV. Because the photosphere of the star is too cool to support this ionization state, the observed gas must be associated

with the circumstellar material. For comparison with WD J0234-0406, we gather together some spectral characteristics of the handful of other white dwarfs that display these lines.

Section 2 presents a discussion of our observations and data reduction. Section 3 summarizes results for circumstellar elements and for those in the photosphere. We discuss these results in Section 4. Section 5 presents the consideration of a few interesting aspects of the spectrum of WD J0234-0406, including the ultraviolet lines of Si IV. Section 6 gives our conclusions.

## 2. OBSERVATIONS AND DATA REDUCTION

Our 2017 discovery of the noteworthy spectrum of WD J0234-0406 was one product of our team's large scale survey to identify heavily accreting white dwarf stars (C. Melis et al. 2018; A. E. Doyle et al. 2023). As may be seen in Table 1, follow up observations with a variety of spectrometers were carried out in 2018, and then, after a break of a year, WD J0234-0406 was extensively observed with HIRES. The GF21 observation of WD J0234-0406 occurred in 2019 January.

### 2.1. *Kast Spectroscopy*

Discovery observations were performed at Lick Observatory with the Kast Double Spectrograph mounted on the Shane 3m telescope. Kast observations simultaneously employed the blue and red arms with light split by the d57 dichroic around 5700 Å. After splitting, blue light was passed through the 600/4310 grism, while red light was passed through the 830/8460 grating. A slit width of  $1.0''$  was used.

Kast data are reduced using standard IRAF long-slit tasks, including bias subtraction, flat-fielding, wavelength calibration with arc lamps, and instrumental response calibration via observations of flux calibration standard stars. Arc lamp frames were not obtained close in time to science frames and as such, the zero-point of the wavelength scale is not accurate. Wavelength ranges covered, resolving powers obtained, and final spectral signal-to-noise ratios are reported in Table 1.

### 2.2. *HIRES Spectroscopy*

WD J0234-0406 was observed with spectrometers on four telescopes (see Table 1). Most of the data were obtained with the HIRES Echelle Spectrometer (S. S. Vogt et al. 1994) on the Keck I telescope at Maunakea Observatory on the UT dates given in Table 1. We used the C5 decker with a slit width of  $1.148''$ . All optical spectra and wavelengths quoted in this paper are in air, corrected to the heliocentric reference frame

Data reduction was performed by using both MAKEE and IRAF following B. Klein et al. (2010) and S. Xu

**Table 1.** Observation Log

UT Date	Instrument	Wavelength Range (Å)	Resolving Power	Exposure (s)	S/N
2017 Dec 9	Kast blue	3450–5475	1300	3600	38
2017 Dec 9	Kast red	5600–7850	3000	3600	47
2018 Jan 1	HIRESb	3113–5944	37000	3300	29
2018 Jul 12	COS	1135–1425	15000	19570	8
2018 Sep 2	COS	1135–1425	15000	19570	8
2018 Oct 15	MagE	3200–8200	7500	2 × 3000	120
2018 Oct 27	HIRESb	3113–5944	37000	3300	14
2020 Sep 13	HIRESb	3113–5944	37000	2 × 1800	36
2020 Oct 7	HIRESr	4720–8990	37500	2 × 3500	75
2020 Oct 8	HIRESb	3113–5944	37000	3600	33
2021 Oct 9	HIRESb	3113–5944	37000	2 × 3600	50

NOTE—Signal-to-noise ratio (S/N) per pixel measured at 1350 Å in COS spectra, at 3850 Å in Kast blue spectra and 5800 Å in red spectra, at 5100 Å in MagE spectra, and at 5100 Å in HIRES spectra. COS spectra displayed in the paper have been smoothed over 5 pixels.

et al. (2014). Typically, we used the spectrum of Feige 34 and similar white dwarfs to calibrate the spectrum of WD J0234-0406.

### 2.3. MagE Spectroscopy

Observations at Las Campanas Observatory with the MagE spectrometer (J. L. Marshall et al. 2008) on the Magellan/Baade telescope were obtained for WD J0234-0406. Table 1 provides important observational and data quality parameters. The spectrograph was used with a  $0''.5$  slit, and data were reduced with the facility Carnegie Python pipeline (D. D. Kelson 2003). With a combination of IRAF and in-house IDL routines we perform relative flux calibration on individual echelle orders with standard star spectra, then merge orders with the application of small flux offsets when needed to bring overlapping order segments into agreement.

### 2.4. Cosmic Origins Spectrograph Spectroscopy

*Hubble Space Telescope* Cosmic Origins Spectrograph (hereafter COS, J. C. Green et al. 2012) observations were obtained for WD J0234-0406 during two visits. Seven spacecraft orbits total were allocated to this target as part of GO program 15461. Observations were performed with the G130M grating centered at a wavelength of 1291 Å and were obtained in the TIME-TAG mode using the  $2.5''$  diameter primary science aperture. Two different FP-POS values were utilized during the observations to minimize fixed pattern noise in the detector while minimizing the impact of Ly- $\alpha$  geocoronal

emission on the detector. This setup yields the spectral resolving power and coverage given in Table 1 and has a gap in spectral coverage from 1274 to 1287 Å.

The raw COS data were processed with the CALCOS pipeline and coadded with the use of the IDL script COADD\_X1D (C. W. Danforth et al. 2010; B. A. Keeney et al. 2012). The final spectrum is flux calibrated and presented in vacuum wavelengths corrected to the heliocentric reference frame.

The final spectral signal-to-noise ratio is reported in Table 1. Following M. Jura et al. (2012), we use the time filter module to extract the night-time portion of the data around the O I lines between 1300 and 1308 Å to mitigate terrestrial day airglow emission. Lower signal-to-noise spectra are obtained for the O I lines between 1300 and 1308 Å as a result of the filtering.

Ultraviolet spectra of WD J0234-0406 reveal a highly broadened and deep Ly $\alpha$  photospheric absorption line. Because of the Ly $\alpha$  line, there is essentially no signal below 1300 Å. This is reminiscent of the significantly broader-than-expected Ly $\alpha$  line found by S. Xu et al. (2017) in white dwarf WD 1425+540. While new models have since been developed that better reproduce ultraviolet hydrogen absorption lines in helium-dominated white dwarf atmospheres (B. T. Gänsicke et al. 2018), such models were not in use when the observations of WD J0234-0406 were planned. The result is that the observed flux is dramatically lower than originally expected, and a much lower signal-to-noise ratio is ob-

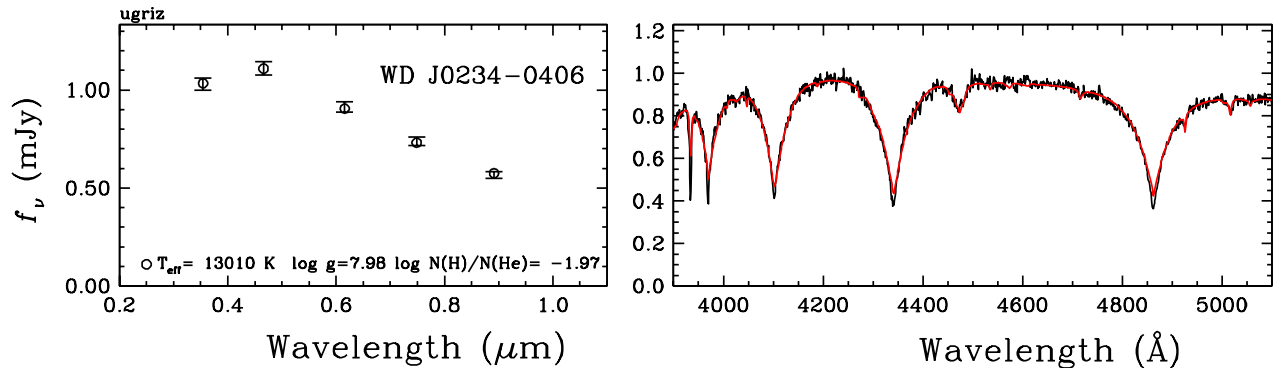


**Figure 1.** Photometric/spectroscopic fit to WD J0234-0406. Left panel: photometric fit (open circles) on SDSS *ugriz* data (error bars). Right panel: Best fit model (red) over the Kast spectrum.

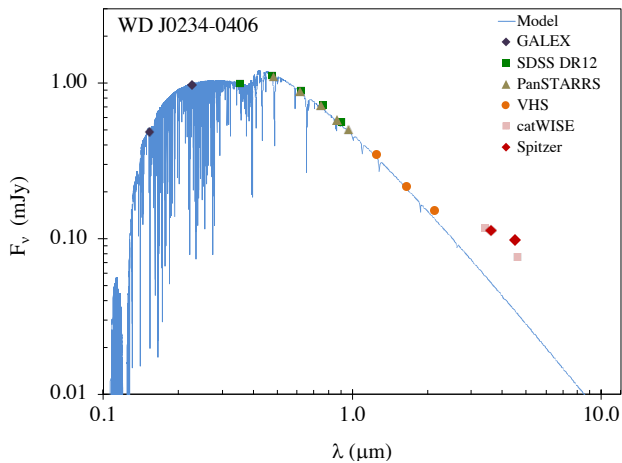


**Figure 2.** Spectral energy distribution of WD J0234-0406. Photometric data from GALEX (L. Bianchi et al. 2017), SDSS (S. Alam et al. 2015), Pan-STARRS (H. A. Flewelling et al. 2020), Two Micron All Sky Survey (2AMSS, R. M. Cutri et al. 2003), VISTA Hemisphere Survey ((R. G. McMahon et al. 2013), and CatWISE (P. R. M. Eisenhardt et al. 2020) surveys. Spitzer data are from S. Lai et al. (2021).

tained than was suggested by preliminary observational planning.

### 2.5. Zwicky Transient Facility Photometry

We queried the ZTF camera at Palomar Observatory (E. C. Bellm et al. 2019; F. J. Masci et al. 2019) for data release 23 to check for photometric variability. Photometry was acquired between July 2018 and December 2024 with the usual seasonal and weather breaks. There were 388, 422 and 71 observations in total in the  $g'$ ,  $r'$  and  $i'$  bands, respectively. The median ZTF  $r'$  and  $g'$  cadence during an observing season was one visit every 2 days.

## 3. METHODS AND MODELS

### 3.1. Photometric Parameters

The spectral energy distribution for WD J0234-0406 is shown in Figures 1 and 2. Excess emission indicative of an orbiting dust disk is evident in Figure 2 in the infrared beginning at a wavelength of about  $2 \mu\text{m}$ , as first reported in A. Rebassa-Mansergas et al. (2019). Minor reddening corrections of GALEX, Sloan Digital Sky Survey (SDSS) and Pan-STARRS photometry were applied with an assumed extinction  $E(B-V) = 0.01$  for a distance of 92 pc. SDSS to AB corrections were made as prescribed by D. J. Eisenstein et al. (2006). Uncertainties in the photometry are close to the size of the data points.

Our best-fit stellar model,  $T_{\text{eff}} = 13,000 \pm 700 \text{ K}$ ,  $\log g = 7.98 \pm 0.03$ , and  $\log(\text{H}/\text{He}) = -1.97 \pm 0.2$ , is presented in Figure 1. The complete physical parameters derived for this white dwarf are listed in Table 2. The GF21 model  $T_{\text{eff}}$  and  $\log g$  for the white dwarf are  $13,454 \pm 200$  and  $8.01 \pm 0.03$ . Their model H/He ratio agrees with ours. Figure 1 of GF21 displays their spectral energy distribution, to which they fit a model dust disk of blackbody temperature 1226 K, with temperature 1872 K at the disk inner edge.

Although the optical spectrum of WD J0234-0406 is dominated by strong Balmer lines, the presence of weak He I lines indicates that the atmosphere of this white dwarf is actually helium-rich, but with a substantial amount of hydrogen – similar to the situation in GD 362 (B. Zuckerman et al. 2007). Using the model atmosphere code described in detail in S. Coutu et al. (2019), we first computed a grid with  $\log g$  between 7.5 and 9.0 in steps of 0.5,  $T_{\text{eff}}$  between 11,000 and 16,000 K in steps of 1000 K, and  $\log(\text{H}/\text{He}) = -1$  to  $-3$  in steps of 0.5.

Since the low-resolution optical spectrum of WD J0234-0406 also shows traces of Ca II H and K lines, heavy elements were included with an initially estimated calcium abundance, chosen based on prior experience and close to the final value (though the exact starting point is not critical). All other elements were scaled to calcium following chondritic proportions. The entire grid was recalculated iteratively until a good match to the photospheric metal lines was achieved; this process included approximately accounting for the contribution of the circumstellar disk during the fitting process (see below, and E. Le Bourdais et al. 2024).

We obtained the atmospheric parameters of WD J0234-0406 by simultaneously fitting the SDSS *ugriz* photometry, trigonometric parallax, and the optical spectrum, using a technique similar to that described in detail in S. Coutu et al. (2019). Because the H abundance in WD J0234-0406 is unusually large for a He atmosphere white dwarf, obtaining a final solution for this abundance necessitated use of photometry, He 4471 Å, and Balmer lines. Interestingly, since the depth of the He I 4471 line is strongly dependent on the H/He ratio, the deduced H/He ratio is driven mostly by a fit to this spectral region.

**Table 2.** Physical parameters of WD J0234-0406.

Parameter	Value
$T_{\text{eff}}$ (K)	$13,010 \pm 710$
$\log g$	$7.98 \pm 0.01$
Mass ( $M_{\odot}$ )	$0.574 \pm 0.008$
$\log \text{H/He}$	$-1.97 \pm 0.2$
Gravitational redshift (km s $^{-1}$ )	$28.6 \pm 0.4$

### 3.2. Gas Disk Model and Photospheric Abundances

We make use of the updated gas disk model presented in E. Le Bourdais et al. (2024) to reproduce the circumstellar features in both the optical and ultraviolet spectra. The disk model is made of 14 confocal eccentric rings evenly spaced radially with each ring having its own density and temperature. An opacity is calculated in each point of the  $50 \times 50 \times 14$  3D grid using TLUSTY and SYNSPEC (I. Hubeny et al. 2021). A Doppler velocity shift is then applied to the opacity to account for the gas rotation and the 3D grid is integrated in the line of sight to obtain 1D opacities as a function of wavelength. The full technical details of the disk model are described at length in P. W. Cauley et al. (2018), M.

Fortin-Archambault et al. (2020) and E. Le Bourdais et al. (2024).

We adjusted the disk’s configuration to reflect the shorter extent of radial velocities in the circumstellar absorption features  $\pm 50 - 100$  km s $^{-1}$  compared to WD 1145+017 ( $\pm 250 - 300$  km s $^{-1}$ ). The configuration was based on the Ti II 3261, 3349 and 3373 Å lines as Ti was the dominant ion in the disk, and the lines were well isolated and uncontaminated by circumstellar absorption lines from other ions. For the disk’s temperature and density, we explored a parameter space ranging from 2500 to 7000 K and from  $1 \times 10^{-14}$  to  $1 \times 10^{-11}$  g/cm $^3$ . We find that the solution most suitable for most of the circumstellar features is a midplane disk temperature of 6000 K and a density of  $9 \times 10^{-14}$  g cm $^{-3}$ . For the disk’s abundances, we started with a CI Chondrite abundance, taking into account the first 30 elements of the periodic table in the model. We then overplotted the combined disk + photosphere model over the spectrum to see how well it matched the circumstellar features. We then adjusted the abundances of the main elements responsible for poorly reproduced features by either increasing the abundance when the feature was too shallow or decreasing when the feature was too deep. The process was done iteratively for all circumstellar features until we obtained an overall satisfying reproduction of all circumstellar features at all wavelengths.

Once the proper disk configuration was obtained, we fitted the photospheric abundances using the method described in E. Le Bourdais et al. (2024).

## 4. RESULTS

### 4.1. Secular Variability

As noted in the Introduction, there has been no measurable variability in the broadband flux from WD J0234-0406. ZTF data were downloaded from the IRSA ZTF DR23 catalog service. Lightcurve data within 5 arcseconds of the stellar position were retrieved. Data points with catalog flags  $> 0$  are removed, as are all observations conducted at an airmass  $\geq 1.8$ . The remaining data points were analyzed. The ZTF photometry yielded  $g'$ ,  $r'$  and  $i'$ -band magnitudes of  $16.344 \pm 0.016$ ,  $16.579 \pm 0.015$  and  $16.827 \pm 0.020$ , respectively. The  $r'$  ZTF observations are shown in Figure 3. For the sake of completeness, we also examined the Transiting Exoplanet Survey Satellite (TESS) 2 minute cadence photometry of WD J0234-0406. TESS observations in Sector 31 (start date of 2020-10-22) covered 25.4 days total with an  $\approx 2.8$  day gap in the middle of the sector. Data were obtained directly from MAST as produced by the Science Processing Operations Center. The TESS observations reveal a flat lightcurve over the monitoring period

with raw rms scatter of  $\sim 25\%$ . Binning the lightcurve produces inter-datapoint scatter closer to what was obtained with ZTF but still reveals no obvious variability.

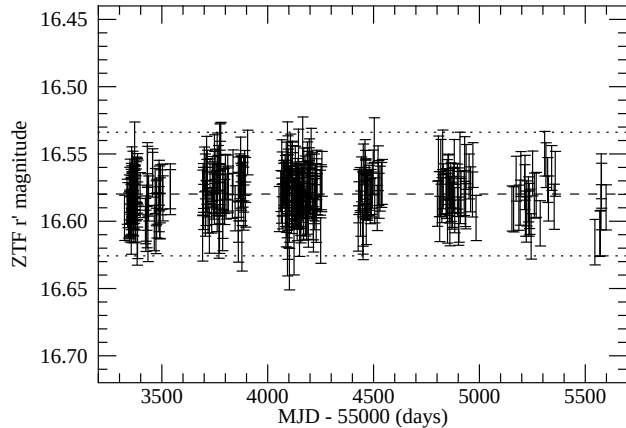


**Figure 3.** ZTF  $r'$  lightcurve for WD J0234-0406. The star appears to be stable with no obvious transit events or variability. Most spectroscopic observations reported in this paper were performed throughout the first half of the displayed lightcurve time range.

No variability is apparent in the circumstellar absorption features. We compared various lines of Fe II and Ti II in HIRESb spectra from three epochs as well as with the HIRESr spectrum in the wavelength region where the b and r spectra overlap (see Table 1). No dramatic changes in line shape or radial velocity of the sort reported in Figure 5 of S. Xu et al. (2019) in WD 1145+017 are apparent in WD J0234-0406. With the caveat that the circumstellar lines are typically broad and weak and often blended with other circumstellar lines or photospheric lines, no variations in radial velocity or EW are noticeable.

That said, secular variability of the sort apparent in WD 1145+017 can come and go (A. Aungwerojwit et al. 2024). Thus, it is possible, albeit unlikely, that short term variations may someday be seen in WD J0234-0406.

#### 4.2. Gaseous Circumstellar Features

Absorption features from the circumstellar gas are distinguished from photospheric lines by the much narrower line widths and somewhat more positive radial velocities of the latter. Some optical transitions display broad/shallow gaseous plus deep/narrow photospheric components, others show only one component (e.g., Figure 4). Figure 5 displays a spectral region dominated by circumstellar gas absorption features. Figure 6 is a comparison between HIRES and MagE spectra. Figures 9 to 12 illustrate our circumstellar model fits to HIRES and COS spectra of WD J0234-0406. The COS resolution is

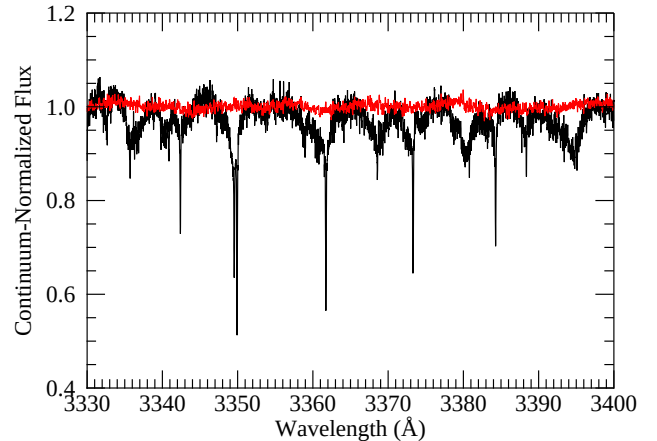


**Figure 4.** WD J0234-0406 (black) vs the featureless white dwarf calibration star EGGR 180 (red). The deep narrow features are photospheric. The shallower, broader, features are circumstellar. Identification of a few prominent lines: 3349.03 and 3349.40 doublet, 3361.21, and 3272.79 Ti II. 3368.04 Cr II. 3380.11 Fe I. 3390 - 3396 is a blend of lines (see Table 4).

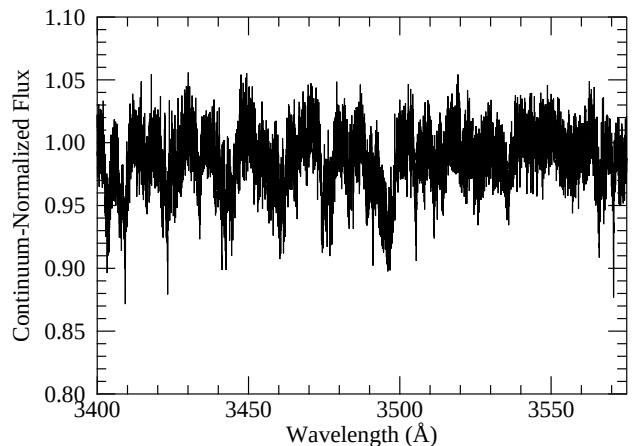


**Figure 5.** Spectral region dominated by circumstellar absorption features.

insufficient to resolve the circumstellar and photospheric components.

GF21 found a few weak emission lines. Specifically, they state: “The only emission features from the gas disc around WD J0234-0406 are the Ca II infrared triplet and the indistinguishable blend of Fe II/Mg I lines near 5175 Å”. There is no mention in GF21 of the broad absorption features that are the focus of this paper. We suspect that this might have been due, at least in part, to an inadequate spectral resolution that ranged between 4000 and 8000. Figure 7 displays the weak Ca IR triplet emission (mentioned by GF21) as measured with HIRES and MagE.

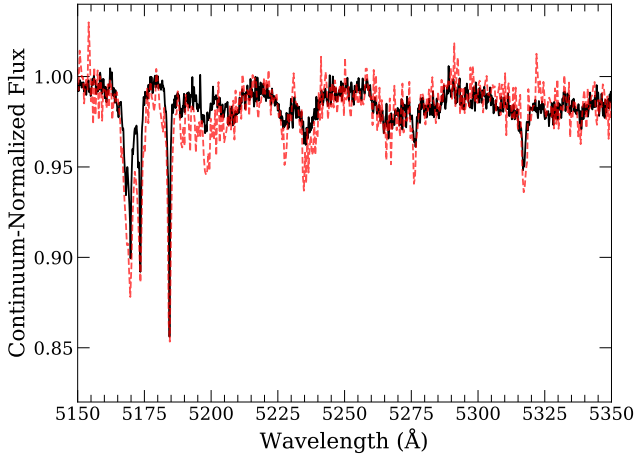


**Figure 6.** Representative HIRES (black), smoothed to match MagE spectral resolution, and MagE (red) spectra showing generally good agreement.

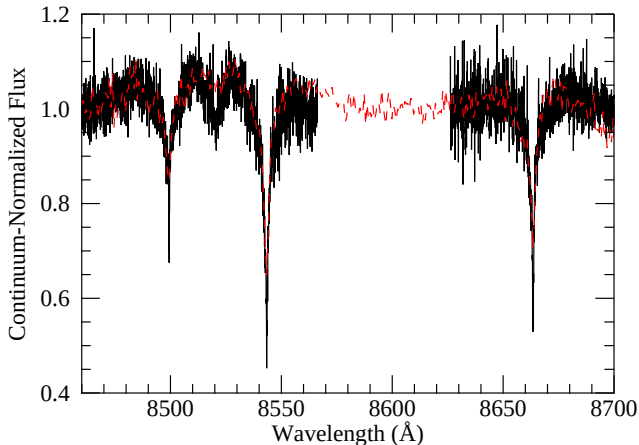


**Figure 7.** Weak Ca IR triplet emission (mentioned by GF21) as measured with HIRES (black) and MagE (red). The dip in the HIRES spectrum at 8520 Å is due to a bad column in the red HIRES detector and not an absorption feature in the white dwarf spectrum.

GF21 note that WD J0234-0406 is the “first white dwarf of spectral type DABZ found to host a gaseous debris disc.” See Section 4.3 for consideration of the spectral classification of WD J0234-0406.

Table 3 presents a list of circumstellar lines present and perhaps present in the spectrum of WD J0234-0406. Because of the broad line widths it is sometimes not possible to decide which of two elements, or perhaps both, is responsible for a given spectral feature. In such cases, transitions of both elements are listed and marked with an asterisk.

In regard to Mg I, photospheric fits to transitions at 3832.30 and 3838.292 Å indicate excess absorption in the

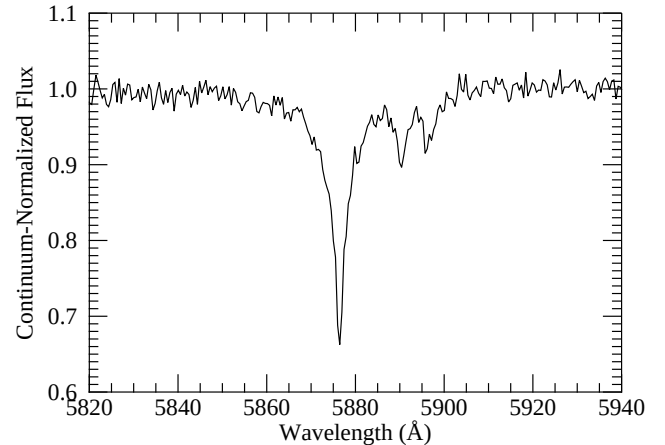


**Figure 8.** Sodium D-lines (5890 and 5896 Å) measured with MagE.

blue wing of the lines, likely consistent with the longer wavelength circumstellar Mg I lines listed in Table 3.

In some portions of the spectra so many gaseous lines are present that they blend together and depress the continuum over a broad range of wavelengths. The most obvious of these wavelength ranges are listed in Table 4. As noted in the table footnote, because laboratory conditions do not match those in the circumstellar gas of WD J0234-0406, the dominant ion identifications given in the table should be regarded as suggestive, rather than definitive. Examples of regions of depressed continuum can be seen in Figures 4 to 6.

A striking aspect of the spectrum of WD J0234-0406 are the Na D1 and D2 lines near 5900 Å, with equivalent width (EW) of 210 and 130 mÅ, respectively (Table 3 and Figure 8). Z. P. Vanderbosch et al. (2021) detect these Na lines with comparable EW, but an order of magnitude smaller linewidths, at white dwarf ZTF J0328-1219. They argue that the Na lines likely originate in circumstellar gas.

**Table 3.** Circumstellar Lines

Ion	$\lambda_o$ (Å)	$\lambda$ (Å)	RV (km s <sup>-1</sup> )	E (eV)	log $gf$	EW (mÅ)	FWHM (Å)
Ca I	4226.728	4226.83	7.2	0	0.24	220	2.9
Ca I	4454.779	4455.31	35.8	1.9	0.24	30	0.8
Ca II	8498.02	8499.09	37.8	1.7	-1.26	1050	6.1
Ca II	8542.09	8542.90	28.4	1.7	-0.31	1650	6.3
Ca II	8662.14	8662.75	21.1	1.7	-0.57	1100	5.4
Cr II	3118.646	3118.90	24.4	2.4	0.00	130	0.9
Cr II	3124.973*	3125.43	43.9	2.4	...	140	0.5
Cr II	3368.05	3368.61	49.9	2.5	-0.09	250	2.0
Cr II	3403.307*	3403.60	25.8	2.4	-0.67	180	1.8
Cr II	3422.732	3423.20	48.0	2.5	-0.41	200	1.7
Cr II	3433.295	3433.66	31.9	2.4	-0.73	120	1.4
Fe I?	3124.885*	3125.43	52.3	3.2	-0.97	140	0.5
Fe I	3136.50	3136.99	46.9	3.3	-0.60	50	0.7
Fe I	3196.927	3197.34	38.8	2.4	0.14	140	1.0
Fe I	3254.362*	3254.68	29.3	3.3	-0.06	50	0.35
Fe I	3380.110*	3380.41	26.6	2.8	-0.70	260	1.6
Fe I	3403.290*	3403.60	27.3	2.8	-1.51	180	1.8
Fe I	3443.876	3444.34	40.4	0.1	-1.37	60	1.6
Fe I	3459.914	3460.45	46.5	3.0	-0.88	150	1.7
Fe I	3513.818	3514.22	34.3	0.9	-1.16	100	1.7
Fe I	3565.379	3566.00	52.2	1.0	-0.13	170	2.0
Fe I	3570.01	3570.46	37.8	2.4	-1.19	40	0.8
Fe I	3581.193*	3581.31	10.0	0.9	0.41	35	0.6
Fe I	3585.319	3585.86	45.3	0.95	-0.80	140	1.6
Fe I?	3593.322*	3593.78	38.2	3.3	...	80	1.1
Fe I	3613.44	3614.03	49.0	3.3	-0.76	90	1.4
Fe I	3618.768	3619.29	43.3	1.0	0.0	80	1.8
Fe I	3631.097	3631.43	27.5	2.8	-0.18	150	1.9
Fe I	3651.467	3651.92	37.2	2.8	0.02	20	0.55
Fe I	3677.628	3678.29	54	2.8	-0.21	130	1.6
Fe I	3694.006	3694.42	33.6	3.0	0.25	30	0.6
Fe I?	3814.523*	3815.18	51.7	1.0	-2.39	180	3.8
Fe I	3820.425	3820.84	32.6	0.9	0.12	120	2.8
Fe I	3859.911	3860.13	17	0	-0.71	40	0.9
Fe I	4132.533*	4133.13	43.3	4.3	-0.86	80	2.0
Fe I	4132.899*	4133.13	16.8	2.8	-1.0	80	2.0
Fe I	4173.315*	4173.76	32.0	2.8	-1.76	150	3.1
Fe I?	4215.423*	4215.94	36.8	3.0	-1.76	120	2.0

**Table 3** *continued*

**Table 3** (*continued*)

Ion	$\lambda_o$ (Å)	$\lambda$ (Å)	RV (km s <sup>-1</sup> )	E (eV)	log <i>gf</i>	EW (mÅ)	FWHM (Å)
Fe I	4289.915*	4290.33	29.0	3.4	-1.54	180	3.0
Fe I	4443.194*	4443.97	52.2	2.9	-0.97	160	3.1
Fe I	5167.488*	5168.05	32.6	1.5	-1.12	20	0.4
Fe I	5586.756	5587.53	41.6	3.4	0.10	250	7:
Fe II	3135.362	3135.75	37.1	3.9	-1.1	120	0.9
Fe II	3183.11	3183.56	42.4	1.7	-2.05	90	0.8
Fe II	3255.886	3256.29	37.2	1.0	-2.45	50	0.5
Fe II	3258.773	3259.26	44.8	3.9	-0.92	100	0.6
Fe II?	3295.819*	3296.1	25.6	1.1	-2.9	180	1.8
Fe II	4173.451*	4173.76	22.2	2.6	-2.16	150	3.1
Fe II	4233.162	4233.70	38.1	2.6	-1.97	70	0.9
Fe II	4385.377*	4385.86	33.0	2.8	-2.59	340	3.3
Fe II	4416.819*	4417.20	25.9	2.8	-2.61	240	3.8
Fe II	4508.28	4508.77	32.6	2.8	-2.37	70	1.4
Fe II	4522.628	4523.03	26.7	2.8	-2.25	50	1.0
Fe II	4549.466*	4550.04	37.9	2.9	-1.73	180	1.4
Fe II	4583.829*	4584.18	23.0	2.8	-1.74	180	2.0
Fe II	4923.921*	4924.69	46.8	2.9	-1.2	340	3.9
Fe II	5018.436	5018.86	25.3	2.9	-1.1	50:	0.5:
Fe II	5169.028	5169.4	21.6	2.9	-1.0	570	5.3
Fe II	5316.609	5317.14	30.5	3.1	-1.87	140	2.0
Mg I	5167.321*	5168.05	42.3	2.7	-0.87	20	0.4
Mg I	5172.68	5173.25	33.0	2.7	-0.45	60	1.7
Mg I	5183.604	5183.94	19.4	2.7	-0.18	60	1.6
Mn II	3441.988	3442.45	40.2	1.8	-0.35	80	0.8
Mn II	3474.1*	3474.52	36.3	1.8	-0.93	100	1.1
Mn II	3482.905	3483.19	24.5	1.8	-0.84	70	1.0
Na I	5889.950	5890.46	26.0	0	0.11	400**	3.0**
Na I	5895.924	5896.32	20.2	0	-0.19	320**	3.0**
O I	~7774	7774.66	Blend	9.1	~0.2	~700	~6
Ti II	3162	Blend of 3	...	0.12	...	300	1.9
Ti II	3190.879	3191.09	19.8	1.1	0.23	20	0.25
Ti II	3217.063	3217.43	34.2	0.027	-0.49	260	1.7
Ti II	3222.843	3223.00	14.6	0.01	-0.42	70	1.0
Ti II	3229.198	3229.53	30.8	0	-0.56	190	1.1
Ti II	3254.247*	3254.68	39.9	0.05	-0.56	50	0.35
Ti II	3261.585	3261.80	19.8	1.89	0.53	30	0.4
Ti II	3271.655	3271.98	29.8	1.24	-0.28	160	1.8
Ti II	3276.772	3277.41	58.4	1.18	-0.89	210	2.3
Ti II	3287.661	3288.25	53.7	1.9	0.46	220	1.5

**Table 3** *continued*

**Table 3** (*continued*)

Ion	$\lambda_o$ (Å)	$\lambda$ (Å)	RV (km s <sup>-1</sup> )	E (eV)	log <i>gf</i>	EW (mÅ)	FWHM (Å)
Ti II	3332.111	3332.55	39.5	1.2	-0.11	60	0.6
Ti II	3349.2	Blend of 2	...	...	...	200	...
Ti II	3372.80	3373.0	18.0	0.01	0.28	110	1.3
Ti II	3380.279*	3380.41	11.6	0.05	-0.63	260	1.6
Ti II	3387.846	3388.29	39.3	0.03	-0.41	120	1.1
Ti II	3407.20	3407.7	43.1	0.05	-2.0	120	1.3
Ti II	3510.845	3511.33	41.4	1.9	0.29	70	0.9
Ti II?	3814.58*	3815.18	47.2	0.6	-1.61	180	3.8
Ti II	3900.551	3901.09	41.4	1.1	-0.20	25	0.5
Ti II	3913.465	3913.95	37.2	1.1	-0.42	60	1.2
Ti II	4395.033	4395.57	36.6	1.1	-0.66	60	1.0
Ti II	4468.50	4469.08	38.9	1.1	-0.60	40	0.7
Ti II	4501.270	4501.69	28.0	1.1	-0.77	60	1.1
Ti II	4533.969	4534.60	41.8	1.2	-0.77	80	1.3
Ti II	4549.617*	4550.04	27.9	1.6	-0.10	180	1.4
Ti II	4571.968	4572.62	42.8	1.6	-0.32	100	1.8
V I?	3295.462*	3296.1	58.1	1.4	-1.92	180	1.8
V I?	3295.78*	3296.1	29.1	1.2	...	180	1.8
V I	4135.296	4135.73	31.5	1.1	-2.0	50	1.2
V I	4385.327*	4385.86	36.5	2.1	-1.0	340	3.3
V I	4416.468*	4417.20	49.7	0.27	-0.83	240	3.8
V I	4434.594	4435.05	30.8	1.9	-0.34	100:	3.0:
V I	4443.336*	4443.97	42.8	2.7	0.36	160	3.1
V I?	4583.78*	4584.18	26.2	1.9	...	180	2.0
V I?	5275.6	5276.08	27.3	2.3	...	140	2.9
Sc II	3572.526	3572.80	23.0	0.02	0.27	60	0.8
Sc II	3576.34	3576.83	41.1	0	0.01	50	1.2
Sc II	3580.925*	3581.31	32.3	0	-0.15	35	0.6
Sc II	4246.822	4247.16	23.9	0.3	0.24	20	0.4
Sr II	4077.71	4078.1	28.7	0	0.15	80	1.1
Sr II	4215.524*	4215.95	30.3	0	-0.17	120	2.0

NOTE—Air rest wavelengths  $\lambda_o$  (A. Kramida et al. 2024; P. A. M. van Hoof 2018);  $\lambda$  measured wavelength; RV radial velocity with respect to the Sun; E lower state energy; EW equivalent width; FWHM full width at half maximum depth. \* indicates line blended with another listed element. Fe I at 3378.679 and 3402.256 appear to be present as does some blend of Fe I 3475.450, 3475.651 & 3476.344. The Fe I line at 3820.425 Å might be blended with photospheric He I at 3819.61 Å. The Fe II line at 4923.921 might be blended with photospheric He I at 4921.93. For Na I, double \* indicates that the EW and FWHM entries are obtained from the MagE spectrum and not from a HIRES spectrum.

The Na lines at WD J0234-0406 are unlikely to be photospheric due to the high temperature of the star.

In addition, the radial velocities of the two lines differ substantially from the velocity of the photosphere (see Section 5). Thus, the Na lines are either circumstellar or

**Table 4.** Regions of Broad Circumstellar Absorption in WDJ0234

Wavelength range (Å)	Dominant Ions	Other Ions
3145–3150	Fe I	V I
3175–3200	Fe I, Fe II	Ti II, V I
3208–3220	Fe I	Fe II, Ti II, V I
3220–3246	Fe I, Ti II	Fe II, V I
3300–3320	Fe I	V I
3320–3330	Fe I	Ti II, V I
3335–3345	Fe I, Ti II, V I	...
3358–3362	Ti II	Fe I, Sc II?
3378–3385	Fe I, Ti II	...
3390–3396	Fe I, Ti II, V I	...
3450–3470	Fe I, V I	Ti II
3641–3652	Fe I, V I	...
3745–3751	Fe I, V I	...
3756–3763	Fe I	Ti II, V I
3784–3802	Fe I, V I	...
3823–3847	Mg I	Fe I, V I
5203–5211	Fe I, V I	...

NOTE—The contributions of the listed ions to the regions where broad absorption of the continuum is noted is based on laboratory data given in [A. Kramida et al. \(2024\)](#) and [P. A. M. van Hoof \(2018\)](#). Because the laboratory conditions do not match those in the circumstellar gas of WD J0234-0406, the dominant ion identifications given here should be regarded as suggestive, rather than definitive. Ca I (circumstellar) might contribute in some wavelength ranges.

interstellar, but very probably the former for the following reasons. Table 1 in [D. M. Sfeir et al. \(1999\)](#) lists 144 stars between 50 and 200+ pc from Earth. WD J0234-0406 is 92 pc from Earth. Of the 144 stars, 62 are within 100 pc – none have D2 EW as large as 120 mÅ. Of the stars beyond 100 pc a few have EW >120 mÅ; the most extreme example by far is HD 188350 at 106 pc and with D2 EW = 218 mÅ. In most directions, the local low-density interstellar solar bubble extends out to <100 pc. The stars closest to WD J0234-0406 in the [D. M. Sfeir et al.](#) table are HD 18543 and HD 18633. These are >100 pc from Earth ( $\rho_i = 8.94$  and 8.61 mas) and about 8 deg away from WD J0234-0406 in the plane of the sky. Both have D2 EW <3.5 mÅ.

Another, even stronger, reason why the Na lines are circumstellar is their line widths (FWHM in Table 3) which are far larger than widths of interstellar Na lines. [L. M. Hobbs \(1978\)](#) presents data for interstellar Na

absorption lines toward 44 stars; the line widths are  $\leq 20$  km s<sup>-1</sup>.

#### 4.3. Photospheric Spectrum and Stellar Classification

The optical spectrum of WD J0234-0406 contains strong photospheric Balmer lines of hydrogen – see Figure 1 above and Figure 2 in GF21. WD J0234-0406 stands out as extremely H-rich among He-dominated white dwarfs with similar effective temperatures (see fig. 5 of [B. Rolland et al. 2018](#)). WD J0234-0406 also displays photospheric neutral helium lines at 4471.50, 5015.68, 5875.70, and 6678.15 Å. He I 3888.65 Å may be present but it is blended with H  $\zeta$  at 3889.05 Å. He I 3819.61 Å may be present but blended with a circumstellar line of Fe I, and He I 4921.93 Å may be present but blended with a circumstellar Fe II line (see note to Table 3). A strong (EW  $\sim 1$  Å), broad, line at about 4715 Å may be He I 4713.2 Å. Even though the He lines are weaker than the H lines, the white dwarf is actually helium-rich, as first noted by GF21.

The optical and ultraviolet spectrum contains numerous photospheric lines from a variety of elements, see Figures 9 to 12 and Tables 5 and 6. The COS resolution is insufficient to resolve (separate) photospheric and circumstellar contributions to a given line. Photospheric abundances are given in Table 7. All optical abundances were derived using HIRES data only. Table 7 also lists the abundances in the photosphere of WD 1145+017 ([E. Le Bourdais et al. 2024](#)) and WD 1425+540 as listed in Table 1 of [S. Xu et al. \(2017\)](#). Based on its element abundances, the parent body accreted onto WD 1425+540 was probably similar to a Kuiper Belt object of our solar system.

GF21 classify WD J0234-0406 as a DABZ, noting that although the star is He-rich the optical lines with the largest EW (by far) are Balmer lines. Since the white dwarf also displays lines from many heavy elements, the question is how to decide whether the secondary type should be DABZ or DAZB. [A. E. Doyle et al. \(2023\)](#), see their Section 3.1) note that the paradigm established in [E. M. Sion et al. \(1983\)](#) and [F. Wesemael et al. \(1993\)](#) states that the spectral type is defined in order of the strongest optical spectral features, but no further definition is given as to what exactly this means. As noted by [A. E. Doyle et al.](#), if “strong” refers to the depth of a line then the strongest line in a given spectrum can depend on linewidth and spectral resolution. Thus they suggest that equivalent width rather than line depth be used to define “line strength”, since EW is independent of line shape. The EW of the 5875.70 Å He I line in WD J0234-0406 is about the same as the EW of the Ca II K-line. Therefore, the DABZ classification by GF21 is reason-

**Table 5.** Optical Photospheric Lines

Ion	Air Wavelength (Å)
Al I	3944.00, 3961.52
Ca I	4226.73
Ca II	3158.87, 3179.33, 3181.78, 3706.02, 3736.90, 3933.66, 3968.47, 8498.02, 8542.09, 8662.14
Cr II	3124.97b, 3132.05, 3368.04, 3408.76, 3422.73, 3433.30
Fe I	3124.89b, 3392.62, 3394.58b, 3570.10, 3581.19, 3608.86, 3618.77, 3677.63, 3719.93, 3734.86, 3749.49, 3758.23, 3759.29, 3761.32, 3763.79, 3767.19, 3815.84, 3820.43, 3825.88, 3827.82, 3834.22, 3855.85b, 3859.91, 4063.59, 4071.74, 4471.70b, 5167.49b, 6820.37?
Fe II	3154.20b, 3167.86, 3193.80, 3196.07, 3210.44, 3213.31, 3227.74, 3258.77, 5018.436, 5169.028
Mg I	3829.36, 3832.30, 3838.29, 5167.32b, 5172.68, 5183.60
Mg II	4481.13, 4481.33
O I	7771.94, 7774.17, 7775.39
Ti II	3154.19b, 3161.77, 3162.57, 3168.52, 3190.88, 3202.53, 3217.05, 3222.84, 3224.24, 3229.19, 3232.28, 3234.51, 3236.57, 3239.04, 3241.98, 3248.60, 3251.91, 3252.91, 3254.25, 3261.58, 3271.66, 3287.66, 3322.93, 3329.45, 3335.19, 3340.34, 3341.87, 3346.75, 3349.03, 3349.40, 3361.21, 3372.79, 3380.28, 3383.76, 3387.83, 3394.58b, 3685.20
V I??	3855.84b

NOTE—Rest Wavelengths: if followed by a "b" indicate a potential blend of two listed elements. See Section 4.3 for a discussion of photospheric lines of He I.

**Table 6.** Ultraviolet Photospheric Lines

Ion	Vacuum Wavelength (Å)
Al II	1189.19, 1190.05, 1191.81, 1211.90
C II	1334.53, 1335.71
Fe II	1112.05, 1121.98, 1122.53, 1128.72, 1138.63, 1142.31, 1143.23, 1144.94, 1147.41, 1148.28, 1151.15, 1169.19, 1175.68, 1183.83, 1198.93, 1224.13, 1230.93, 1260.53, 1266.68, 1267.42, 1271.98, 1272.61, 1275.78, 1277.64, 1296.70, 1358.94, 1361.38, 1368.09, 1371.02, 1375.17, 1379.47, 1392.82, 1408.48, 1412.84, 1424.72
Mg II	1239.93, 1240.40
Ni II	1133.73, 1134.53, 1137.09, 1154.42, 1164.58, 1168.04, 1171.29, 1317.22, 1335.20, 1370.13, 1381.29, 1411.07
O I	1152.15, 1217.65, 1302.17, 1304.86, 1306.03
Si I	1258.80
Si II	1190.42, 1193.29, 1194.50, 1197.39, 1223.90, 1224.25, 1226.80, 1226.98, 1227.60, 1228.61, 1228.74, 1229.34, 1246.74, 1248.43, 1250.09, 1240.44, 1251.16, 1260.42, 1264.74, 1265.00, 1304.37, 1309.28, 1346.88, 1348.54, 1350.07, 1352.64, 1353.72
Si III	1113.23, 1206.5, 1294.55, 1296.73, 1298.95

able. Perhaps it is now time, 40 years on from the initial Sion et al paper, for the appearance of a new paper devoted to establishment of a white dwarf classification scheme (e.g. O. Vincent et al. (2025)).

#### 4.4. Parent Body Composition and Mass

Elements heavier than helium settle out of white dwarf stellar photospheres in times much shorter than white

dwarf cooling times (ages). Settling times are functions of the white dwarf effective temperature, surface gravity, and atmospheric composition, the latter usually assumed to be either pure H or pure He. As noted in Section 3.1, the atmosphere of WD J0234-0406 is composed primarily of He, but with an unusually large fractional abundance of H. The presence of so much H substantially shortens the photospheric lifetime of heavy ele-

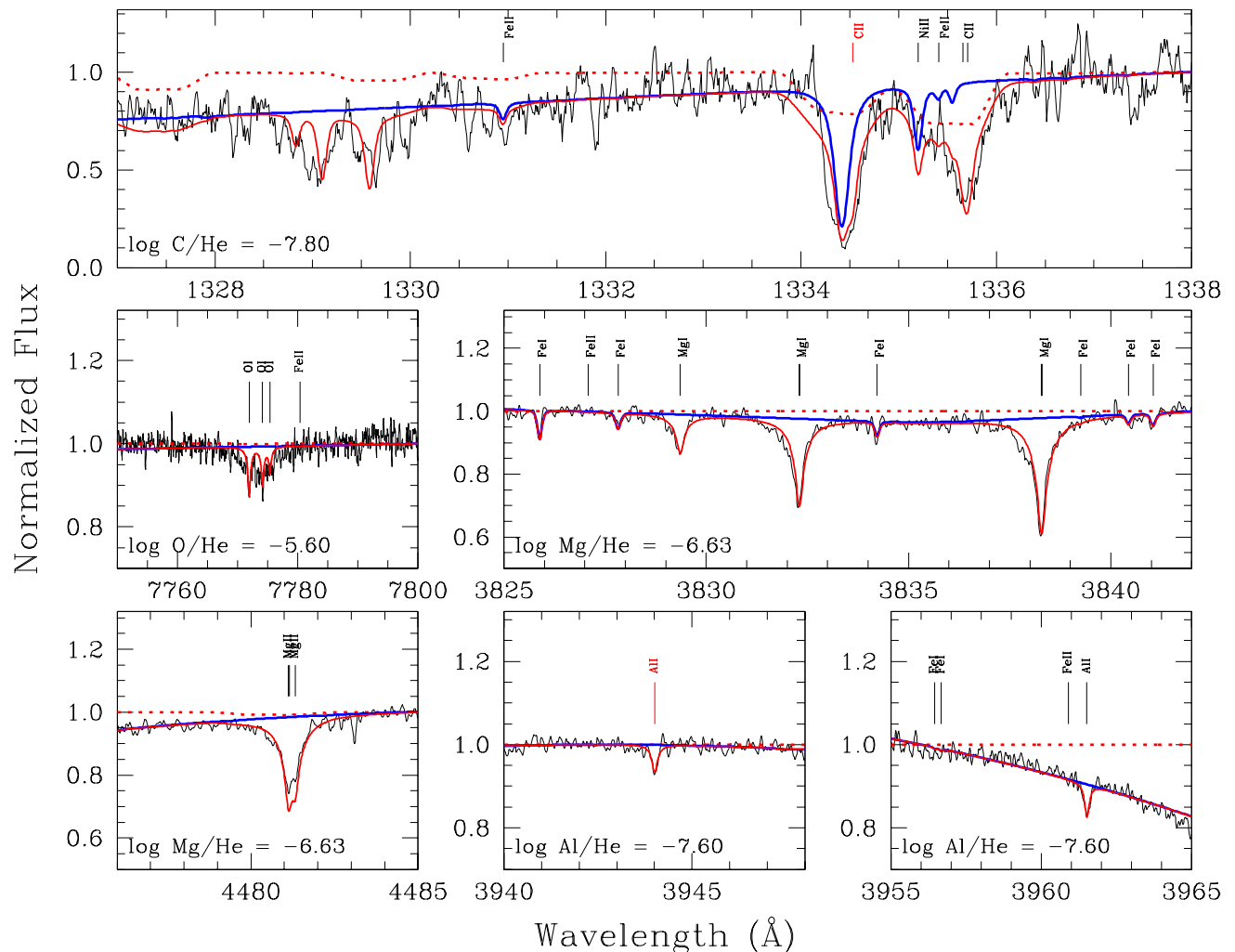


**Figure 9.** Selected regions of the photospheric fit (red) to WD J0234-0406 and its circumstellar disk (dotted red). The model photospheric + circumstellar gas spectrum without the fitted photospheric element is shown in blue. A red label is used for lines coming from the ground state.

ments compared to what these lifetimes would be in a pure He atmosphere (see Table 8).

As noted in the Introduction, WD J0234-0406 and WD 1145+017 presently are the only white dwarfs to display broad circumstellar absorption lines. Figure 13 illustrates how much deeper, typically, the broad absorption lines are in WD 1145+017 compared to WD J0234-0406. The entries in Table 7 show that heavy elements are substantially more abundant in the photosphere of WD 1145+017; this is especially true for S, Fe, and Ni. For comparison, photospheric abundances for the Kuiper Belt like object accreted onto WD 1425+540 are also listed. The Table 7 entries are displayed graphically in Figure 14.

WD J0234+0406 has a prominent circumstellar disk so either of two accretion situations are plausible. The so-called “increasing phase” (Incr. Phase column in Table 8) pertains to the early stages of accretion of material from disk onto star; here there has been insufficient time for any accreted element to diffuse out of the convective zone and into the stellar interior. Based on the calculated settling times for the mixed H/He atmosphere (Figure 15), the increasing phase should last for a few times  $10^5$  years. The increasing phase is followed by the steady state (St. State in Table 8) where the rate of accretion of additional photospheric material from the disk is balanced by the rate at which heavy elements settle into the white dwarf interior and out of sight.

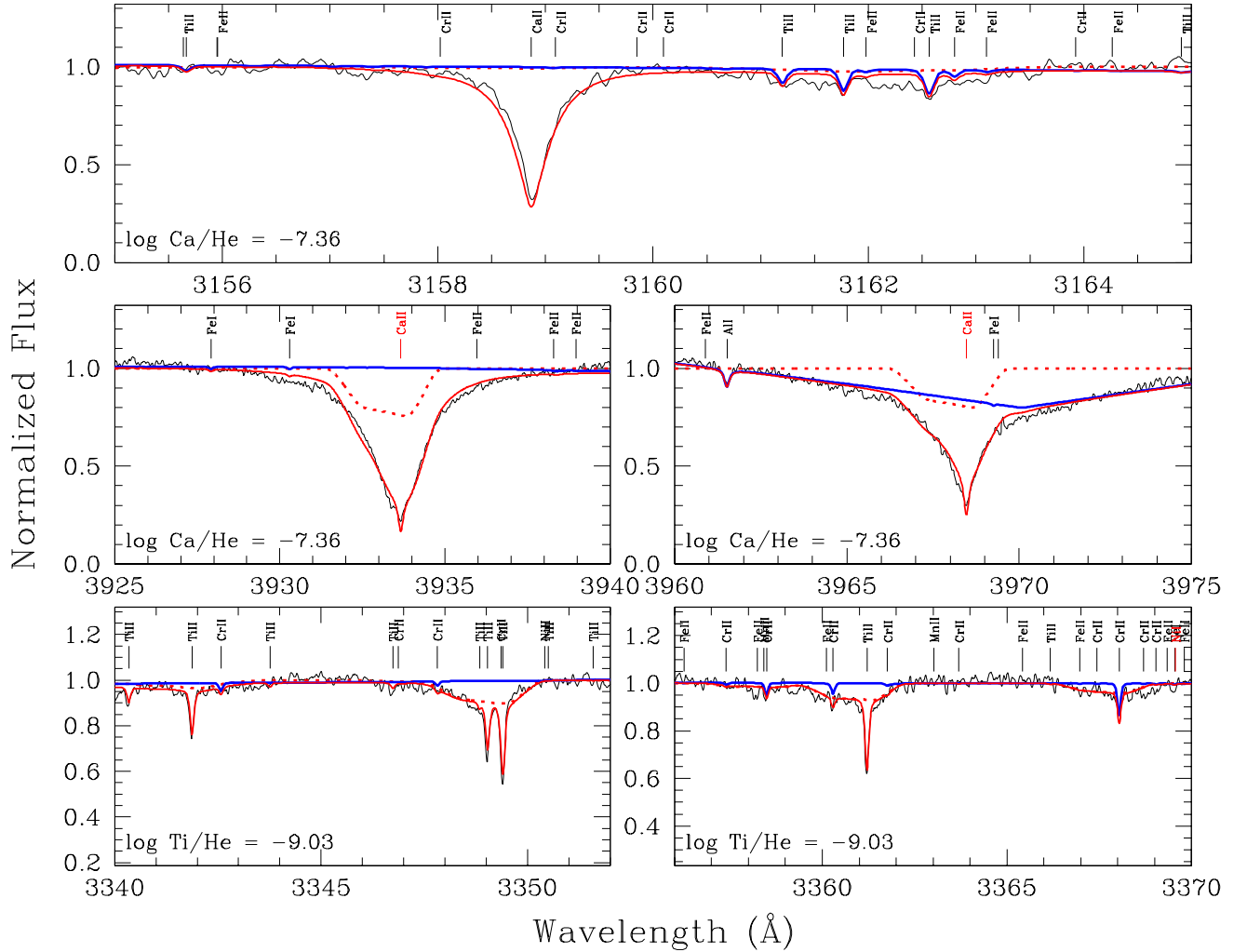


**Figure 10.** Selected regions of the photospheric fit (red) to WD J0234-0406. In dotted red is the expected contribution of the circumstellar gas disk for the velocity profile that matches best the Ti features (see Section 3.2). The model photospheric + circumstellar gas spectrum without the fitted photospheric element is shown in blue. A red label is used for lines coming from the ground state.

The settling times listed in the fourth column of Table 8 are an average of the two sets of calculated settling times displayed in Figure 15. The mass of the star in these models is 0.59 times the mass of the sun. For the Koester model, the log of the mass of the convective zone as a fraction of the stellar mass is -6.096, while for the Montreal model it is -6.345. These are roughly an order of magnitude smaller than the mass of the convective zone in a white dwarf with a pure He atmosphere and the same temperature and  $\log g$  as WD J0234-0406.

We used two independent codes to calculate settling timescales for an atmospheric hydrogen abundance 1% by number that of helium. One code is based on the method originally described in C. Paquette et al. (1986), with updates presented in G. Fontaine et al. (2015) and

R. A. Heinonen et al. (2020). This is the same framework used for the pure H and pure He timescales provided in the Montreal White Dwarf Database (P. Dufour et al. 2017). The other code is that described in D. Koester et al. (2020). Both calculations assume no overshoot of the convection zone. We find that the presence of so much H substantially reduces the extent of the convection zone and thus shortens the photospheric lifetimes of heavy elements compared to the case of a pure He envelope. While the difference between settling times in the two models is about a factor of two, the agreement in relative settling times between two metals – which is most important for the interpretation – is significantly better.

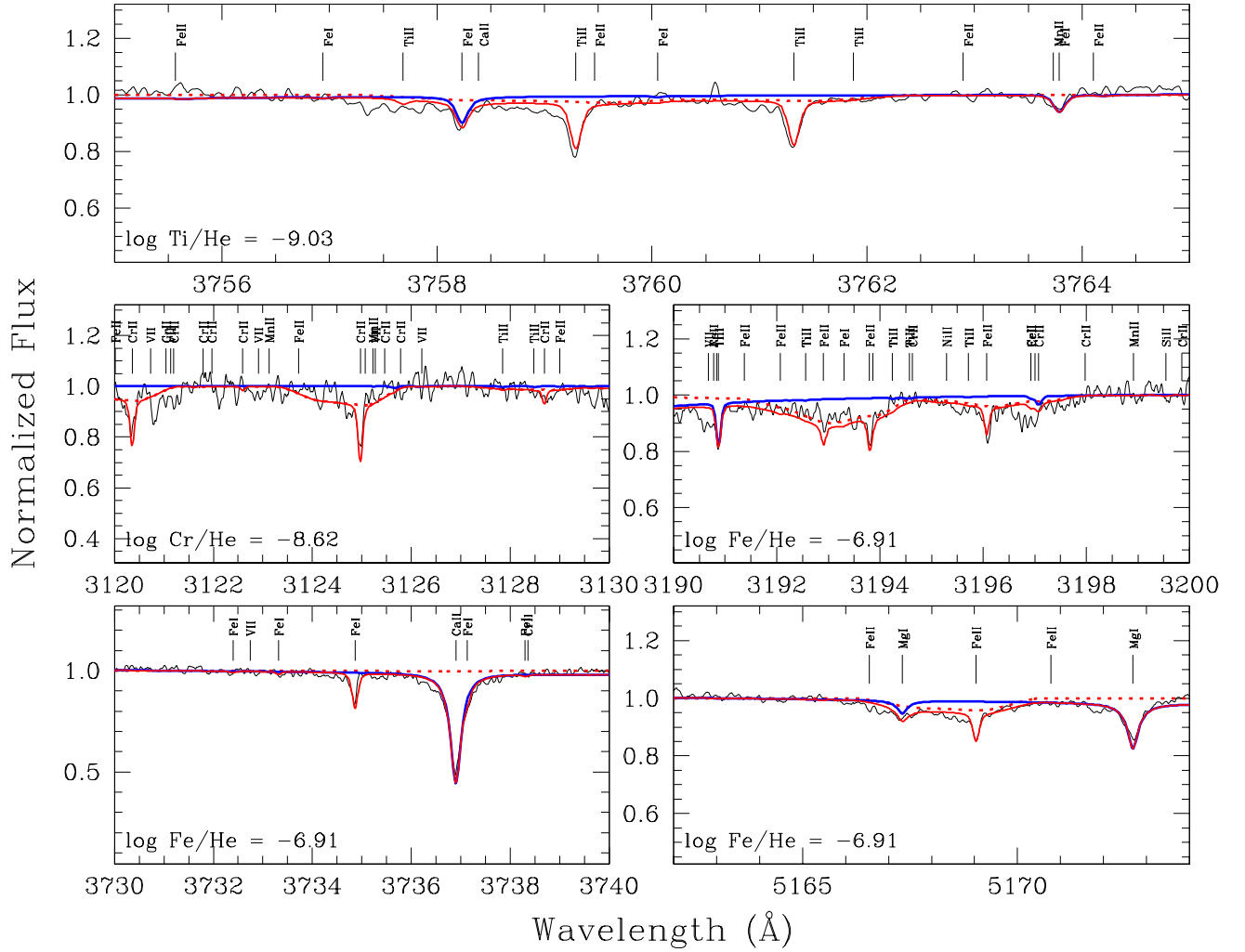


**Figure 11.** Selected regions of the photospheric fit (red) to WD J0234-0406 and its circumstellar disk (dotted red). The model photospheric + circumstellar gas spectrum without the fitted photospheric element is shown in blue. A red label is used for lines coming from the ground state.

The bottom row of Table 8 gives the “oxygen budget”. A detailed discussion of how the uncertainties in the oxygen budget are calculated may be found in Section 4.3 of B. Klein et al. (2010). As noted in the last sentence of the caption to Table 8, the listed oxygen budgets of less than unity indicate that the parent body for the material currently seen in the photosphere contained a substantial quantity of water. Given the error bars on the oxygen budget, a dry parent body appears quite unlikely, but can’t be ruled out with certainty. The unusually large percentage (1%) of H in WD J0234+0406 contrasts with that seen in other white dwarfs with He dominated atmospheres; the H percentages listed in Table 7 for WD 1145+017 and WD 1425+540 are much more typical. Because, by number, H is 4 orders of mag-

nitude more abundant than O, only a tiny fraction of the H in the atmosphere of WD J0234-0406 could have been carried by the parent body responsible for the heavy elements now seen in the photosphere. Most of the H must have accompanied previously accreted objects or have been present when the white dwarf formed or, more likely, both. According to simulations of H transport in He-rich white dwarfs, primordial H likely contributes but cannot fully account for such a large photospheric abundance, thus requiring an external source (B. Roland et al. 2018; A. Bédard et al. 2023).

The current heavy element mass contained in the convective zone gives a lower limit to the mass of the parent body. This heavy element convective zone mass is about  $10^{22}$  g which is rather smaller than the minimum

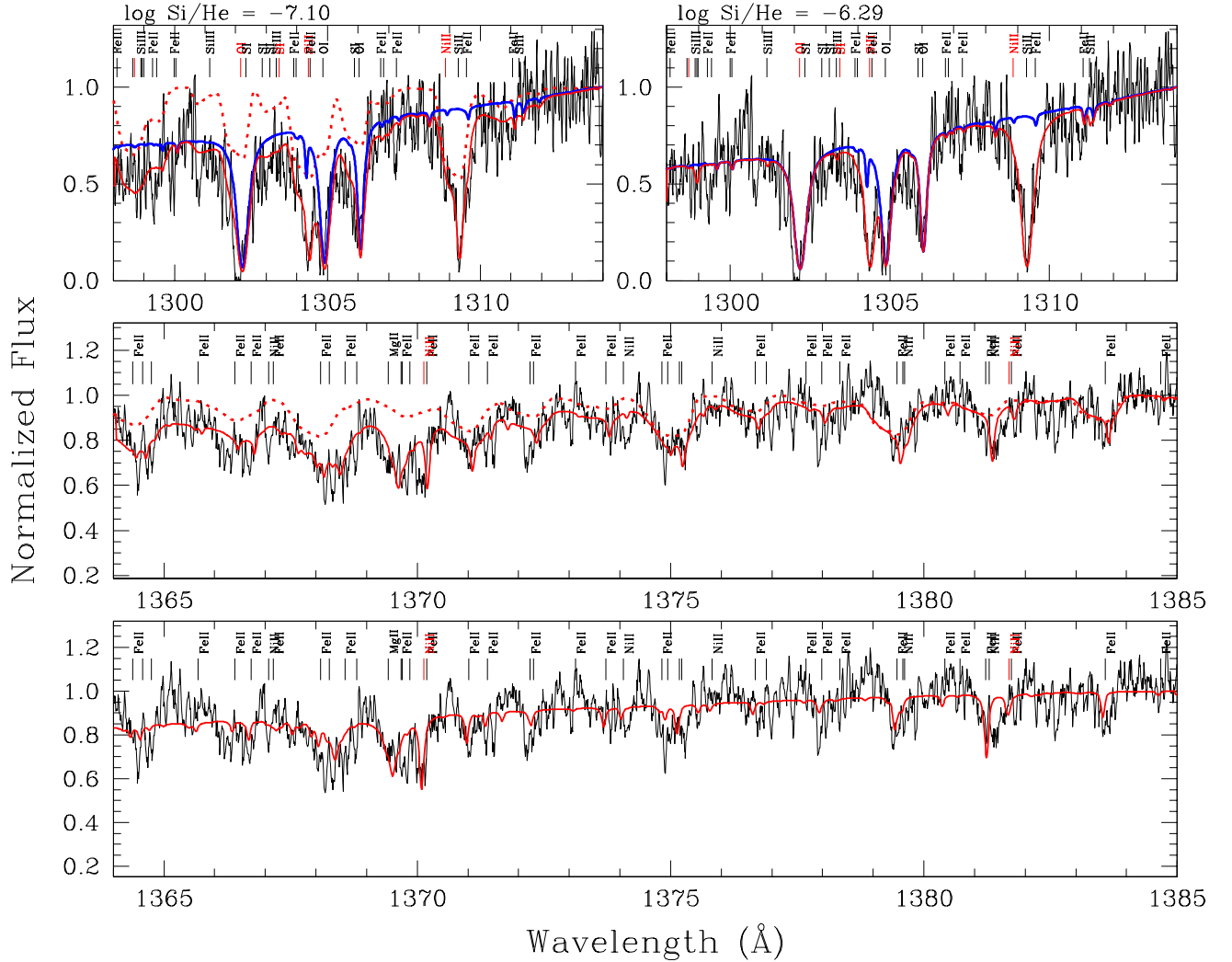


**Figure 12.** Top left: Photospheric fit (red) of silicon lines in the UV, including the circumstellar disk (dotted red). Top right: Traditional photospheric fit (red) of silicon lines in the UV. The obtained Si abundance with (left) and without (right) including the disk are presented over the top two panels. The blue line represents the photosphere without silicon. Bottom: Selected region of the UV with (green) and without the contribution of the disk to the continuum. The rest wavelengths of the OI lines in the top two panels are 1302.17, 1304.86, and 1306.03 Å.

parent body mass given for many He atmosphere white dwarfs (e.g., WD 1145+017). But much of the difference can be accounted for by the relatively small mass of the WD J0234-0406 convective zone – as noted two paragraphs above.

E. Le Bourdais et al. (2024) conclude that in WD 1145+017 “both the disk and photosphere compositions align, to first order, with CI Chondrite.” The same appears to be the case for WD J0234-0406; however the parent body of WD 1145+017 apparently had a more prominent Ni-Fe core than that of WD J0234-0406. In addition, the volatile elements S and C in WD J0234-0406 are substantially less abundant than in chondritic material. Some models of Earth’s core include these ele-

ments, although more commonly O and/or Si (K. Hirose et al. 2021).

## 5. DISCUSSION

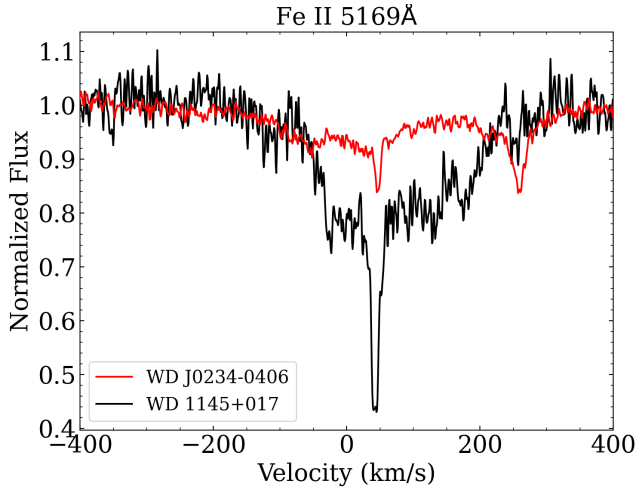
### 5.1. Optical Thickness

At least some gaseous emission lines at white dwarf stars appear to be optically thick (e.g., B. T. Gänsicke et al. 2006; K. Horne & T. R. Marsh 1986). Many of the circumstellar absorption lines at WD J0234-0406 are also likely to be optically thick formed by gas that covers  $\leq 10\%$  of the star because the circumstellar lines are never more than about 10% deep, and lines with large EW are broader (Table 3), consistent with optical thickness. For WD 1145+017, S. Redfield et al. (2017) argue that the circumstellar lines are not very optically thick

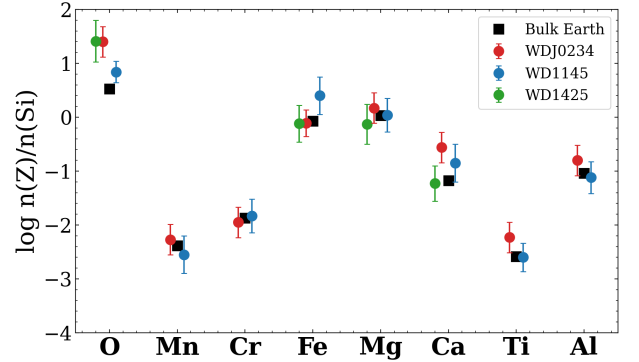
**Table 7.** Photospheric Abundances in WD J0234-0406, WD 1145+017 and WD 1425+540.

Element	WD J0234 (opt) log n(Z)/n(He)	WD J0234 (UV) log n(Z)/n(He)	WD 1145 (opt) log n(Z)/n(He)	WD 1145 (UV) log n(Z)/n(He)	WD 1425 log n(Z)/n(He)
Hydrogen	-1.97±0.20	...	-4.83±0.14	...	-4.20±0.10
Beryllium	< -11.5	...	...	...	...
Carbon	...	-7.80±0.30	...	-7.39±0.29	-7.29±0.17
Nitrogen	...	< -7.0	...	...	-8.09±0.10
Oxygen	-5.60±0.20	-6.10±0.30	-4.95±0.14	-5.43±0.35	-6.62±0.23
Sodium	< -8.0	...	< -6.0	...	...
Magnesium	-6.63±0.20	...	-5.75±0.28	-5.98±0.26	-8.16±0.20
Aluminum	-7.60±0.20	...	-6.91±0.26	-6.71±0.16	...
Silicon	-6.80±0.20	-7.09±0.10	-5.79±0.14	-5.69±0.28	-8.03±0.31
Phosphorus	...	< -6.0	...	-7.30±0.33	...
Sulfur	...	< -9.2	...	-6.33±0.36	-8.36±0.11
Calcium	-7.36±0.20	...	-6.64±0.32	...	-9.26±0.10
Titanium	-9.03±0.20	...	-8.39±0.22	...	...
Vanadium	< -10.0	...	-9.01±0.40	...	...
Chromium	-8.75±0.20	...	-7.62±0.28	...	...
Manganese	-9.07±0.20	...	-8.34±0.32	...	...
Iron	-6.91±0.14	-7.33±0.20	-5.39±0.32	-5.46±0.31	-8.15±0.14
Nickel	...	-8.41±0.20	-6.61±0.37	-6.79±0.32	-9.67±0.20

NOTE—WD 1145+017 abundances from *E. Le Bourdais et al. (2024)*. WD 1425+540 abundances from *S. Xu et al. (2017)*.

**Figure 13.** Fe II 5169 Å.

based on correlation of EW with  $\log gf$  for Fe II lines (their Figure 4). Inspection of Fe and Ti lines in our Table 3 yields no obvious such correlation or correlation with lower state energy ( $E$  in Table 3).

**Figure 14.** Abundances comparison.

## 5.2. Radial Velocities

*J. H. Debes et al. (2012)* report a white dwarf with a weak, narrow, circumstellar Ca II K line blueshifted by  $\sim 30 \text{ km s}^{-1}$  from the photospheric line; they interpret the velocity offset as due to gravitational redshift of the latter line. The circumstellar gas is traveling in a circular orbit with radius equal to 54 times the radius of a white dwarf.

For WD J0234-0406 with the temperature and gravity given in Section 3.1, the evolutionary models of *A.*

**Table 8.** Abundances and Parent Body Mass Compositions

Z	$\log(n(Z)/n(\text{He}))$	$\log \tau(Z)$		% mass composition			
		(yrs)	(yrs)	Incr. Phase	St. State	CI chondrites	Bulk Earth
		Pure He	He+H mix	Any H/He	He+H mix		
H	$-1.97 \pm 0.20$	...	...	...	...	...	...
Be	$< -11.50$	6.391	5.679	...	...	$2.2 \times 10^{-6}$	$4.6 \times 10^{-6}$
C	$-7.80 \pm 0.30$	6.342	5.653	$0.49^{+0.49}_{-0.25}$	$0.36^{+0.36}_{-0.18}$	4.13	0.17
N	$< -7.00$	6.283	5.626	...	...	0.25	0.0013
O	$-5.85 \pm 0.30$	6.271	5.609	$58.3^{+58.0}_{-29.1}$	$47.5^{+47.2}_{-23.7}$	45.4	32.4
Na	$< -8.00$	6.258	5.536	...	...	0.51	0.19
Mg	$-6.63 \pm 0.20$	6.276	5.534	$14.7^{+8.6}_{-5.4}$	$14.2^{+8.3}_{-5.3}$	9.5	15.8
Al	$-7.60 \pm 0.20$	6.266	5.479	$1.7^{+1.0}_{-0.6}$	$1.9^{+1.1}_{-0.7}$	0.84	1.5
Si	$-6.95 \pm 0.20$	6.280	5.466	$8.2^{+4.8}_{-3.0}$	$9.3^{+5.4}_{-3.4}$	10.8	17.1
P	$< -6.00$	6.252	5.424	...	...	0.10	0.07
S	$< -9.20$	6.230	5.411	...	...	5.4	0.46
Ca	$-7.36 \pm 0.20$	6.099	5.372	$4.5^{+2.6}_{-1.7}$	$6.3^{+3.7}_{-2.3}$	0.88	1.6
Ti	$-9.03 \pm 0.20$	6.051	5.320	$0.12^{+0.07}_{-0.04}$	$0.18^{+0.11}_{-0.07}$	0.05	0.08
V	$< -10.00$	6.046	5.308	...	...	0.005	0.009
Cr	$-8.75 \pm 0.20$	6.062	5.313	$0.24^{+0.14}_{-0.09}$	$0.38^{+0.23}_{-0.14}$	0.26	0.42
Mn	$-9.07 \pm 0.20$	6.061	5.296	$0.12^{+0.07}_{-0.04}$	$0.20^{+0.12}_{-0.07}$	0.19	0.14
Fe	$-7.12 \pm 0.21$	6.079	5.291	$10.9^{+6.8}_{-4.2}$	$18.5^{+11.5}_{-7.1}$	18.6	28.8
Ni	$-8.41 \pm 0.20$	6.101	5.274	$0.59^{+0.34}_{-0.22}$	$1.04^{+0.61}_{-0.38}$	1.10	1.7
Oxygen Budget				$0.46 \pm 0.21$	$0.65 \pm 0.29$		

NOTE—Abundances adopted for O, Si and Fe are the average of optical and UV derived values.  $\tau(Z)$  in the pure He column are the settling times in a  $T_{\text{eff}} = 13,000$  K,  $\log g = 7.98$  WD atmosphere from the MWDD (P. Dufour et al. 2017) in units of  $\log(\text{years})$ . The  $\log \tau(Z)$  listed in the He+H mix column are obtained from the average of the two settling times shown in Figure 15. The  $\log \tau(Z)$  Pure He column is included here to illustrate to what degree the presence of a substantial abundance of hydrogen in the convection zone reduces the settling times. The compositions by mass in the four columns on the right are the following: “Incr. Phase” = directly observed abundance ratios, “St. State” = abundance ratios corrected for differential element settling, “CI chondrites” = meteoritic abundances from K. Lodders (2021), “bulk Earth” = compositions by mass from C. Allègre et al. (2001). As defined in B. Klein et al. (2010), an oxygen budget less than 1 implies there is excess oxygen not accounted for by rocky oxides (most likely originating from water in the parent body).

Bédard et al. (2020) predict a gravitational redshift of  $28.6 \pm 0.4$  km s<sup>-1</sup>. We measured the radial velocity of the photosphere of WD J0234-0406 using a few strong, uncontaminated lines of Ca II, Ti II, Fe I and Mg I. The velocities of all elements agree to within a km s<sup>-1</sup> or so of each other. We adopt  $46 \pm 1$  km s<sup>-1</sup> as the velocity of the photosphere, of which  $28.6 \pm 0.4$  km s<sup>-1</sup> is the gravitational redshift (Table 2).

To measure the radial velocity of the circumstellar gas we used 12 lines of Fe I, 8 lines of Ti II, 4 lines each of Cr II and Fe II, and one line each of Ca I and V I; all lines had EW  $\geq 90$  mÅ. Because the circumstellar features are weak and broad the standard deviations of the measured velocities for the 4 ions with multiple measured lines are

large; these standard deviations range between about 7 and 10 km s<sup>-1</sup>. Of course the standard errors are much smaller than the standard deviations. In all cases, the velocities of the different ions agree with each other within the errors. We adopt  $40 \pm 2$  km s<sup>-1</sup> as the radial velocity of the circumstellar gas, while admitting the possibility that the radial velocities of different elements might differ from each other.

Thus the measured difference in radial velocity between the photospheric and circumstellar gas is about 6 km s<sup>-1</sup>, which is much less than the gravitational redshift of 28.6 km s<sup>-1</sup>. This small measured velocity difference is likely a consequence of more circumstellar gas along the line of sight to the star streaming away from

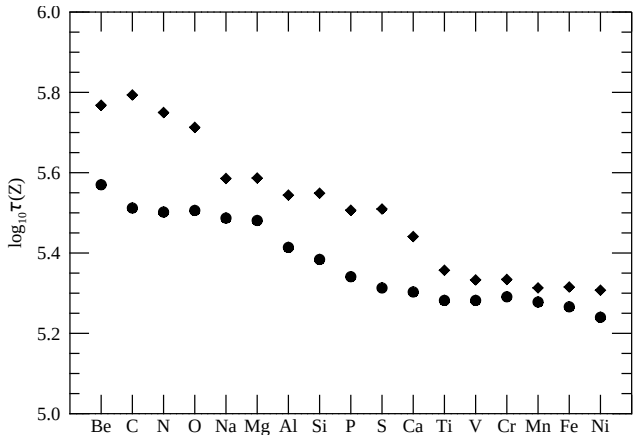


**Figure 15.** Settling times in years for WD J0234–0406 as calculated using the Koester (diamonds) and Montreal (circles) white dwarf envelope codes. The differences in the settling times are mostly due to the different convective zone depths included in the two models.

Earth than toward it. This is consistent with the broad linewidths that imply very non-circular gas orbits (e.g., Figure 4 in *M. Fortin-Archambault et al. 2020*). Indeed, the circumstellar features seen at WD 1145+017 can be redshifted with respect to the photospheric lines (see, e.g., Figure 1 in *S. Xu et al. (2016)* or Figure 5 in *S. Xu et al. (2019)*), notwithstanding the gravitational redshift of the latter lines.

### 5.3. Si IV

Two transitions of Si IV are seen in absorption in the COS spectrum of WD J0234-0406 (Figure 16 and Table 9). The existence of substantial numbers of Si I ions in this high state of ionization at the 13,000 K photospheric temperature of this star is incompatible with our atmospheric models. In addition, the  $\sim 700$  mÅ full linewidth at half maximum intensity is far larger than the FWHM of photospheric lines and is characteristic of the circumstellar gas. Thus, the Si IV lines must be associated in some way with circumstellar material. According to the published literature and research currently underway (see Table 9), we are aware of a total of 11 white dwarfs with effective temperature  $< 23,000$  K that display these Si IV lines. Discussion of their significance and interpretation appears in Section 7 of *B. T. Gänsicke et al. (2012)* and Section 3.2 of *L. K. Rogers et al. (2024)*.

As noted in Section 5.1, optical circumstellar lines are never deeper than about 10% of the stellar continuum, while in the UV the COS resolution is insufficient to cleanly separate circumstellar and photospheric line contributions. But the Si IV lines originate only in the circumstellar gas and, as may be seen in Fig-

ure 16, their depth is substantially greater than 10%. Thus the Si IV ions must occlude a large fraction of the disk of the star and may be optically thick. The Si IV lines in PG 0843+516 *B. T. Gänsicke et al. (2012)* and Gaia J0006+2858 *L. K. Rogers et al. (2024)* are also very deep indicating substantial optical depth and fractional coverage of the stellar disk. The close-in Si IV disk gas apparently covers more of the star than does more distant gas evident in other ions.

As noted in *B. T. Gänsicke et al. (2012)*, the Si IV spectrum of WD 1226+110 (= SDSS 1228+1040) is composed of two absorption components, one in the photosphere and a weaker, blueshifted, one carried by gaseous circumstellar material. The COS spectrum was obtained in 2010. The circumstellar feature is no longer present in COS spectra obtained in 2016, 2017 and 2018 (*C. Manser 2024, personal communication*). If, as seems plausible, the Si IV absorption is due to the hottest portion of a ring of circumstellar gas, then this hot material may have precessed away from the line of sight between Earth and WD 1226+110.

Table 9 reveals some regularities in the characteristics of the ensemble of detected Si IV lines. For a few of the hotter white dwarfs, the Si IV radial velocities are sometimes similar to those of the stellar photospheres thus suggesting possible origin in the photosphere. But usually Si IV is blue-shifted with respect to the photosphere, whatever the photospheric temperature. If the blue-shift is small then the Si IV may be formed in a hot gaseous layer with nearly circular orbit close to the star (*B. T. Gänsicke et al. 2012*). Here, the difference in radial velocities could be due entirely to a somewhat larger gravitational redshift of the photosphere compared to the orbiting Si IV ions. But WD 0408-041 and SDSS J1957+3404 have Si IV blue-shifts of order 40 km s<sup>-1</sup>. So, either the Si IV lines are somehow formed far enough from the stars so that there is negligible gravitational redshift or a kinematic component, i.e. some non-circular orbital motion, must be present. Such a situation is dramatically seen in Gaia J0006+2858 where Si IV absorption is blue-shifted from the photosphere by about 220 km s<sup>-1</sup> (*9* and *L. K. Rogers et al. 2024*). This large shift combined with the modest width of this blue-shifted line (not smeared out in velocity as in circumstellar material at WD J0234-0406 and WD 1145+017) suggests some kind of elliptical ring of material that passes close to Gaia J0006+2858.

## 6. CONCLUSIONS

Previously, only one white dwarf (WD 1145+017) with broad circumstellar absorption lines (100s of km/s wide) has appeared in the literature (*S. Xu et al. 2016*).

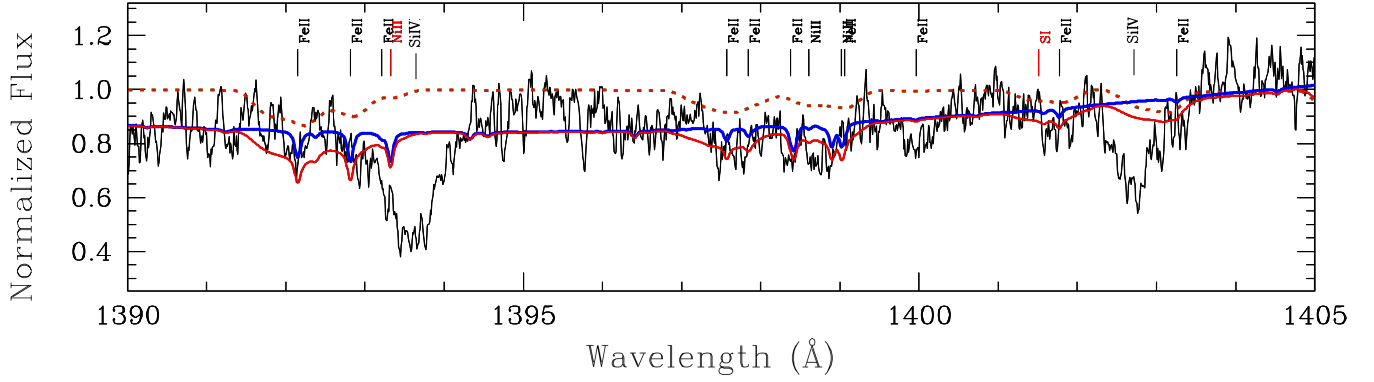


**Figure 16.** Si IV lines present in the spectrum of WD J0234-0406 at 1394 Å and 1403 Å. The line colors have the same meaning as in previous figures.

**Table 9.** Si IV Absorption Lines

Star	Atm.	$T_{\text{eff}}$ (K)	$\log g$	Dist (pc)	RV Phot (km/s)	1394 Å RV (km/s)	1394 Å EW (mÅ)	1403 Å RV (km/s)	1403 Å EW (mÅ)	Ref.
Gaia J0006+2858	H	22,840	7.86	152	23.8	-196	...	-196	...	(1)
Gaia J0006+2858	H	22,840	7.86	152	23.8	20	213 (36)	25.6	122 (45)	(1)
WD J0234-0406	He	13,000	7.98	91	46	-7.5	538	29.9	425	(2)
Gaia J0347+1624	H	18,850	7.84	141	16.0	...	...	...	...	(1)
WD 0408-041	H	15,270	8.09	72	13.0	-20.6	580	-21.3	405	(1, 1*)
Gaia J0510+2315	H	20,130	8.13	65	26.1	...	...	...	...	(1)
Gaia J0611-6931	H	16,530	7.81	143	58.7	...	...	...	...	(1)
Gaia J0644-0352	He	17,000	7.98	112	93.2	...	...	...	...	(1)
Gaia J0649-7624	H	21,910	8.09	144	32.6	29.9	76	28.9	58	(3)
WD 0843+516	H	23,097	8.17	139	1.2	-13.5	826	-13.5	600	(4)
PG 1015+161	H	19,200	8.22	88	77.4	...	...	...	...	(4)
SDSS J1043+0855	H	18,330	8.05	169	39.0	...	...	...	...	(5)
WD 1145+017	He	15,500	8.19	146	25	-15	22	-15	16	(6, 7)
WD 1226+110	H	20,900	8.15	129	41.3	...	...	...	...	(4*)
WD 1622+587	He	21,530	7.98	183	-23.0	-23.4	94	-23.7	72	(1)
GALEX J1931+0117	H	21,200	7.91	53	38.0	30.7	540	30.7	330	(4)
SDSS J1957+3404	H	17,955	8.12	128	-30.0	-73.8	800	-70.1	490	(8)
Gaia J2100+2122	H	22,000	7.92	88	4.7	...	...	...	...	(1)

NOTE—References: (1) [L. K. Rogers et al. \(2024\)](#); (1\*) [L. K. Rogers \(2025, private communication\)](#); (2) this paper; (3) [I. L. Trierweiler et al. \(2025\)](#); (4) [B. T. Gänsicke et al. \(2012\)](#); (4\*) See text, Section 5.3; (5) [C. Melis & P. Dufour \(2017\)](#); (6) [M. Fortin-Archambault et al. \(2020\)](#); (7) [E. Le Bourdais et al. \(2024\)](#); (8) [C. Melis \(2025, private communication\)](#).

This paper presents a second such example: WD J0234-0406. In order to account for the large linewidths the orbits of the circumstellar material must be substantially non-circular. In WD 1145+017 the line profile changes dramatically with time ([M. Fortin-Archambault et al. 2020](#); [P. W. Cauley et al. 2018](#)), shifting from redshifted to blueshifted with respect to the photosphere. This has been modeled as due to precessing rings of high velocity gas ([J. Budaj et al. 2022,](#)

and references therein). Dramatic variations are also seen in the depths of dips in the broadband flux from WD 1145+017. However, no obvious secular variations are seen in the spectrum of WD J0234-0406 – neither photometric nor spectroscopic. Notwithstanding such differences, for WD J0234-0406 we utilized a gas disk model updated from that used by [E. Le Bourdais et al. \(2024\)](#) for analysis of WD 1145+017. The best fitting disk model indicates the presence of ions of at least a

dozen different elements. None of the circumstellar absorption features (with the exception of two UV lines of Si IV) appears to be deeper than about 10% of the continuum. Thus, the main portion of the circumstellar disk probably covers only about 10% of the face of the white dwarf.

The elemental composition of the parent body responsible for the observed photospheric heavy elements, as well as the dusty/gaseous disk, appears to have been similar to that of CI chondrites, but with a lower abundance of volatile elements, specifically S and C. Of interest is whether the parent body carried a substantial quantity of water; to determine this we used a technique first employed by [B. Klein et al. \(2010\)](#) for He atmosphere white dwarfs. Our conclusion is that the parent body was likely quite “wet”, although given the size of the error bars on the abundances of the relevant elements, a dry parent body can’t be ruled out with certainty.

The photosphere of WD J0234+0406 is helium dominated, but with an unusually high fractional abundance of hydrogen (1% by number). This represents so much H that even if the object currently being accreted was wet, its water content can account for only a minority of the hydrogen in the photosphere of the star. Therefore, the bulk of the observed H was obtained from parent bodies that accreted onto the star long ago, or is primordial, or both.

Si IV lines are seen in the ultraviolet spectrum of WD J0234-0406; given the relatively low (13,000 K) temperature of the star these lines must be formed in the circumstellar material and not in the stellar photosphere. We have gathered existing Si IV spectra from other white dwarfs of which we are aware for comparison with WD J0234-0406. For some of the hotter stars, the Si IV lines might be formed in the stellar photosphere, but in most cases, more likely, from hot circumstellar material that orbits near the white dwarf. For a few stars, including WD J0234-0406, the Si IV lines appear to be formed in a layer of hot gas in an elliptical orbit that passes close to the stellar photosphere. In WD J0234-0406 and some other white dwarfs the Si IV absorption lines are very deep indicating that the absorbing gas must cover a major portion of the face of the star plus the Si line optical depths must be substantial.

White dwarf stars now known to be accreting material onto their photospheres from their surrounding planet systems number more than 1700 ([J. T. Williams et al.](#)

[2024](#)), a number that will soon greatly increase: “The forthcoming DESI DR1 sample contains over 47 000 white dwarf candidates, and will revolutionize statistical studies of white dwarf samples.” ([C. J. Manser et al. 2024](#)). The number of candidate exoplanets around main sequence stars is of order 7000<sup>9</sup>. Typically, the white dwarfs sample stars more massive and older than the main-sequence stars along with planetary material with larger orbital semi-major axes.

#### ACKNOWLEDGMENTS

We thank the referee for comments/suggestions that helped to improve the paper. We are grateful to Boris Gänsicke, Snehalata Sahu, Chris Manser, and Laura Rogers for kindly supplying us with unpublished data or calculations and we thank Edward Young and Jay Farahi for helpful advice. C.M. and B.Z. acknowledge support from NSF grants SPG-1826583 and SPG-1826550. B.K. acknowledges support from NASA grant HST-GO-16204.005-A to UCLA.

This paper is based on observations made with the NASA/ESA Hubble Space Telescope, obtained at the Space Telescope Science Institute, which is operated by the Association of Universities for Research in Astronomy, Inc., under NASA contract NAS 5-26555. This work was supported by the associated grant HST-GO-15461.001-A. Research at Lick Observatory is partially supported by a generous gift from Google. This paper includes data gathered with the 6.5 m Magellan Telescopes located at Las Campanas Observatory, Chile.

Some of the data presented herein were obtained at the W.M. Keck Observatory, which is operated as a scientific partnership among the California Institute of Technology, the University of California, and NASA. The Observatory was made possible by the generous financial support of the W. M. Keck Foundation. We recognize and acknowledge the very significant cultural role and reverence that the summit of Maunakea has always had within the indigenous Hawaiian community. S. Xu is supported by the international Gemini Observatory, a program of NSF NOIRLab, which is managed by the Association of Universities for Research in Astronomy (AURA) under a cooperative agreement with the US National Science Foundation, on behalf of the Gemini partnership of Argentina, Brazil, Canada, Chile, the Republic of Korea, and the United States of America.

<sup>9</sup> <https://exoplanetarchive.ipac.caltech.edu/>

## REFERENCES

- Alam, S., Albareti, F. D., Allende Prieto, C., et al. 2015, *ApJS*, 219, 12, doi: [10.1088/0067-0049/219/1/12](https://doi.org/10.1088/0067-0049/219/1/12)
- Allègre, C., Manhès, G., & Lewin, E. 2001, *E&PSL*, 185, 49, doi: [10.1016/S0012-821X\(00\)00359-9](https://doi.org/10.1016/S0012-821X(00)00359-9)
- Aungwerojwit, A., Gänsicke, B. T., Dhillon, V. S., et al. 2024, *MNRAS*, 530, 117, doi: [10.1093/mnras/stae750](https://doi.org/10.1093/mnras/stae750)
- Bédard, A., Bergeron, P., & Brassard, P. 2023, *ApJ*, 946, 24, doi: [10.3847/1538-4357/acbb62](https://doi.org/10.3847/1538-4357/acbb62)
- Bédard, A., Bergeron, P., Brassard, P., & Fontaine, G. 2020, *ApJ*, 901, 93, doi: [10.3847/1538-4357/abafbe](https://doi.org/10.3847/1538-4357/abafbe)
- Bellm, E. C., Kulkarni, S. R., Graham, M. J., et al. 2019, *PASP*, 131, 018002, doi: [10.1088/1538-3873/aaecbe](https://doi.org/10.1088/1538-3873/aaecbe)
- Bianchi, L., Shiao, B., & Thilker, D. 2017, *ApJS*, 230, 24, doi: [10.3847/1538-4365/aa7053](https://doi.org/10.3847/1538-4365/aa7053)
- Budaj, J., Maliuk, A., & Hubeny, I. 2022, *A&A*, 660, A72, doi: [10.1051/0004-6361/202141924](https://doi.org/10.1051/0004-6361/202141924)
- Cauley, P. W., Farihi, J., Redfield, S., et al. 2018, *ApJ*, 852, L22, doi: [10.3847/2041-8213/aaa3d9](https://doi.org/10.3847/2041-8213/aaa3d9)
- Coutu, S., Dufour, P., Bergeron, P., et al. 2019, *ApJ*, 885, 74, doi: [10.3847/1538-4357/ab46b9](https://doi.org/10.3847/1538-4357/ab46b9)
- Cutri, R. M., Skrutskie, M. F., van Dyk, S., et al. 2003, 2MASS All Sky Catalog of point sources. <https://ui.adsabs.harvard.edu/abs/2003tmc..book....C>
- Danforth, C. W., Keeney, B. A., Stocke, J. T., Shull, J. M., & Yao, Y. 2010, *ApJ*, 720, 976, doi: [10.1088/0004-637X/720/1/976](https://doi.org/10.1088/0004-637X/720/1/976)
- Debes, J. H., Kilic, M., Faedi, F., et al. 2012, *ApJ*, 754, 59, doi: [10.1088/0004-637X/754/1/59](https://doi.org/10.1088/0004-637X/754/1/59)
- Dennihi, E., Xu, S., Lai, S., et al. 2020, *ApJ*, 905, 5, doi: [10.3847/1538-4357/abc339](https://doi.org/10.3847/1538-4357/abc339)
- Doyle, A. E., Desch, S. J., & Young, E. D. 2021, *ApJ*, 907, L35, doi: [10.3847/2041-8213/abd9ba](https://doi.org/10.3847/2041-8213/abd9ba)
- Doyle, A. E., Klein, B. L., Dufour, P., et al. 2023, *ApJ*, 950, 93, doi: [10.3847/1538-4357/acbd44](https://doi.org/10.3847/1538-4357/acbd44)
- Dufour, P., Blouin, S., Coutu, S., et al. 2017, 509, 3, doi: [10.48550/arXiv.1610.00986](https://doi.org/10.48550/arXiv.1610.00986)
- Eisenhardt, P. R. M., Marocco, F., Fowler, J. W., et al. 2020, *ApJS*, 247, 69, doi: [10.3847/1538-4365/ab7f2a](https://doi.org/10.3847/1538-4365/ab7f2a)
- Eisenstein, D. J., Liebert, J., Harris, H. C., et al. 2006, *ApJS*, 167, 40, doi: [10.1086/507110](https://doi.org/10.1086/507110)
- Farihi, J. 2016, *NewAR*, 71, 9, doi: [10.1016/j.newar.2016.03.001](https://doi.org/10.1016/j.newar.2016.03.001)
- Flewelling, H. A., Magnier, E. A., Chambers, K. C., et al. 2020, *ApJS*, 251, 7, doi: [10.3847/1538-4365/abb82d](https://doi.org/10.3847/1538-4365/abb82d)
- Fontaine, G., Brassard, P., Dufour, P., & Tremblay, P. E. 2015, in , 113. <https://ui.adsabs.harvard.edu/abs/2015ASPC..493..113F>
- Fortin-Archambault, M., Dufour, P., & Xu, S. 2020, *ApJ*, 888, 47, doi: [10.3847/1538-4357/ab585a](https://doi.org/10.3847/1538-4357/ab585a)
- Gänsicke, B. T., Koester, D., Farihi, J., et al. 2012, *MNRAS*, 424, 333, doi: [10.1111/j.1365-2966.2012.21201.x](https://doi.org/10.1111/j.1365-2966.2012.21201.x)
- Gänsicke, B. T., Koester, D., Farihi, J., & Toloza, O. 2018, *MNRAS*, 481, 4323, doi: [10.1093/mnras/sty2526](https://doi.org/10.1093/mnras/sty2526)
- Gänsicke, B. T., Marsh, T. R., Southworth, J., & Rebassa-Mansergas, A. 2006, *Sci*, 314, 1908, doi: [10.1126/science.1135033](https://doi.org/10.1126/science.1135033)
- Gentile Fusillo, N. P., Manser, C. J., Gänsicke, B. T., et al. 2021, *MNRAS*, 504, 2707, doi: [10.1093/mnras/stab992](https://doi.org/10.1093/mnras/stab992)
- Green, J. C., Froning, C. S., Osterman, S., et al. 2012, *ApJ*, 744, 60, doi: [10.1088/0004-637X/744/1/6010.1086/141956](https://doi.org/10.1088/0004-637X/744/1/6010.1086/141956)
- Heinonen, R. A., Saumon, D., Daligault, J., et al. 2020, *ApJ*, 896, 2, doi: [10.3847/1538-4357/ab91ad](https://doi.org/10.3847/1538-4357/ab91ad)
- Hirose, K., Wood, B., & Vočadlo, L. 2021, *NRvEE*, 2, 645, doi: [10.1038/s43017-021-00203-6](https://doi.org/10.1038/s43017-021-00203-6)
- Hobbs, L. M. 1978, *ApJS*, 38, 129, doi: [10.1086/190550](https://doi.org/10.1086/190550)
- Horne, K., & Marsh, T. R. 1986, *MNRAS*, 218, 761, doi: [10.1093/mnras/218.4.761](https://doi.org/10.1093/mnras/218.4.761)
- Hubeny, I., Prieto, C. A., Osorio, Y., & Lanz, T. 2021, doi: [10.48550/ARXIV.2104.02829](https://doi.org/10.48550/ARXIV.2104.02829)
- Jura, M., Muno, M. P., Farihi, J., & Zuckerman, B. 2009, *ApJ*, 699, 1473, doi: [10.1088/0004-637X/699/2/1473](https://doi.org/10.1088/0004-637X/699/2/1473)
- Jura, M., Xu, S., Klein, B., Koester, D., & Zuckerman, B. 2012, *ApJ*, 750, 69, doi: [10.1088/0004-637X/750/1/69](https://doi.org/10.1088/0004-637X/750/1/69)
- Jura, M., & Young, E. D. 2014, *AREPS*, 42, 45, doi: [10.1146/annurev-earth-060313-054740](https://doi.org/10.1146/annurev-earth-060313-054740)
- Keeney, B. A., Danforth, C. W., Stocke, J. T., France, K., & Green, J. C. 2012, *PASP*, 124, 830, doi: [10.1086/667392](https://doi.org/10.1086/667392)
- Kelson, D. D. 2003, *PASP*, 115, 688, doi: [10.1086/375502](https://doi.org/10.1086/375502)
- Klein, B., Jura, M., Koester, D., Zuckerman, B., & Melis, C. 2010, *ApJ*, 709, 950, doi: [10.1088/0004-637X/709/2/950](https://doi.org/10.1088/0004-637X/709/2/950)
- Koester, D., Gänsicke, B. T., & Farihi, J. 2014, *A&A*, 566, A34, doi: [10.1051/0004-6361/201423691](https://doi.org/10.1051/0004-6361/201423691)
- Koester, D., Kepler, S. O., & Irwin, A. W. 2020, *A&A*, 635, A103, doi: [10.1051/0004-6361/202037530](https://doi.org/10.1051/0004-6361/202037530)
- Kramida, A., Yu. Ralchenko, Reader, J., & and NIST ASD Team. 2024, NIST Atomic Spectra Database (ver. 5.12), [Online]. Available: <https://physics.nist.gov/asd>. National Institute of Standards and Technology, Gaithersburg, MD.
- Lai, S., Dennihy, E., Xu, S., et al. 2021, *ApJ*, 920, 156, doi: [10.3847/1538-4357/ac1354](https://doi.org/10.3847/1538-4357/ac1354)
- Le Bourdais, E., Dufour, P., & Xu, S. 2024, *ApJ*, 977, 93, doi: [10.3847/1538-4357/ad90b7](https://doi.org/10.3847/1538-4357/ad90b7)
- Lodders, K. 2021, *SSRv*, 217, 44, doi: [10.1007/s11214-021-00825-8](https://doi.org/10.1007/s11214-021-00825-8)

- Manser, C. J., Gänsicke, B. T., Izquierdo, P., et al. 2024, *MNRAS*, 531, L27, doi: [10.1093/mnras/slaf026](https://doi.org/10.1093/mnras/slaf026)
- Marshall, J. L., Burles, S., Thompson, I. B., et al. 2008, in , eprint: arXiv:0807.3774, 701454, doi: [10.1117/12.789972](https://doi.org/10.1117/12.789972)
- Masci, F. J., Laher, R. R., Rusholme, B., et al. 2019, *PASP*, 131, 018003, doi: [10.1088/1538-3873/aae8ac](https://doi.org/10.1088/1538-3873/aae8ac)
- McMahon, R. G., Banerji, M., Gonzalez, E., et al. 2013, *Msngr*, 154, 35. <https://ui.adsabs.harvard.edu/abs/2013Msngr.154...35M>
- Melis, C., & Dufour, P. 2017, *ApJ*, 834, 1, doi: [10.3847/1538-4357/834/1/1](https://doi.org/10.3847/1538-4357/834/1/1)
- Melis, C., Klein, B., Doyle, A. E., et al. 2020, *ApJ*, 905, 56, doi: [10.3847/1538-4357/abbdfa](https://doi.org/10.3847/1538-4357/abbdfa)
- Melis, C., Zuckerman, B., Dufour, P., Song, I., & Klein, B. 2018, *RNAAS*, 2, 64, doi: [10.3847/2515-5172/aacf41](https://doi.org/10.3847/2515-5172/aacf41)
- Paquette, C., Pelletier, C., Fontaine, G., & Michaud, G. 1986, *ApJS*, 61, 197, doi: [10.1086/191112](https://doi.org/10.1086/191112)
- Rebassa-Mansergas, A., Solano, E., Xu, S., et al. 2019, *MNRAS*, 489, 3990, doi: [10.1093/mnras/stz2423](https://doi.org/10.1093/mnras/stz2423)
- Redfield, S., Farihi, J., Cauley, P. W., et al. 2017, *ApJ*, 839, 42, doi: [10.3847/1538-4357/aa68a0](https://doi.org/10.3847/1538-4357/aa68a0)
- Rogers, L. K., Bonsor, A., Xu, S., et al. 2024, *MNRAS*, 527, 6038, doi: [10.1093/mnras/stad3557](https://doi.org/10.1093/mnras/stad3557)
- Rolland, B., Bergeron, P., & Fontaine, G. 2018, *ApJ*, 857, 56, doi: [10.3847/1538-4357/aab713](https://doi.org/10.3847/1538-4357/aab713)
- Sfeir, D. M., Lallement, R., Crifo, F., & Welsh, B. Y. 1999, *A&A*, 346, 785. <https://ui.adsabs.harvard.edu/abs/1999A&A...346..785S>
- Sion, E. M., Greenstein, J. L., Landstreet, J. D., et al. 1983, *ApJ*, 269, 253, doi: [10.1086/161036](https://doi.org/10.1086/161036)
- Steele, A., Debes, J., Xu, S., Yeh, S., & Dufour, P. 2021, *ApJ*, 911, 25, doi: [10.3847/1538-4357/abc262](https://doi.org/10.3847/1538-4357/abc262)
- Trierweiler, I. L., Melis, C., Le Bourdais, E., et al. 2025, *ApJ*, 993, 53, doi: [10.3847/1538-4357/ae003d](https://doi.org/10.3847/1538-4357/ae003d)
- van Hoof, P. A. M. 2018, *Galax*, 6, 63, doi: [10.3390/galaxies6020063](https://doi.org/10.3390/galaxies6020063)
- Vanderbosch, Z. P., Rappaport, S., Guidry, J. A., et al. 2021, *ApJ*, 917, 41, doi: [10.3847/1538-4357/ac0822](https://doi.org/10.3847/1538-4357/ac0822)
- Vanderburg, A., Johnson, J. A., Rappaport, S., et al. 2015, *Nature*, 526, 546, doi: [10.1038/nature15527](https://doi.org/10.1038/nature15527)
- Veras, D. 2016, *RSOS*, 3, 150571, doi: [10.1098/rsos.150571](https://doi.org/10.1098/rsos.150571)
- Veras, D. 2021, in *Oxford Research Encyclopedia of Planetary Science*, 1, doi: [10.1093/acrefore/9780190647926.013.238](https://doi.org/10.1093/acrefore/9780190647926.013.238)
- Vincent, O., Bergeron, P., & Dufour, P. 2025, *MNRAS*, 538, 2233, doi: [10.1093/mnras/staf448](https://doi.org/10.1093/mnras/staf448)
- Vogt, S. S., Allen, S. L., Bigelow, B. C., et al. 1994, in , 362, doi: [10.1117/12.176725](https://doi.org/10.1117/12.176725)
- Wesemael, F., Greenstein, J. L., Liebert, J., et al. 1993, *PASP*, 105, 761, doi: [10.1086/133228](https://doi.org/10.1086/133228)
- Williams, J. T., Gänsicke, B. T., Swan, A., et al. 2024, *A&A*, 691, A352, doi: [10.1051/0004-6361/202450509](https://doi.org/10.1051/0004-6361/202450509)
- Xu, S., Jura, M., Dufour, P., & Zuckerman, B. 2016, *ApJ*, 816, L22, doi: [10.3847/2041-8205/816/2/L22](https://doi.org/10.3847/2041-8205/816/2/L22)
- Xu, S., Jura, M., Koester, D., Klein, B., & Zuckerman, B. 2014, *ApJ*, 783, 79, doi: [10.1088/0004-637X/783/2/79](https://doi.org/10.1088/0004-637X/783/2/79)
- Xu, S., Zuckerman, B., Dufour, P., et al. 2017, *ApJ*, 836, L7, doi: [10.3847/2041-8213/836/1/L7](https://doi.org/10.3847/2041-8213/836/1/L7)
- Xu, S., Hallakoun, N., Gary, B., et al. 2019, *AJ*, 157, 255, doi: [10.3847/1538-3881/ab1b36](https://doi.org/10.3847/1538-3881/ab1b36)
- Zuckerman, B., Koester, D., Melis, C., Hansen, B. M., & Jura, M. 2007, *ApJ*, 671, 872, doi: [10.1086/522223](https://doi.org/10.1086/522223)
- Zuckerman, B., Koester, D., Reid, I. N., & Hünsch, M. 2003, *ApJ*, 596, 477, doi: [10.1086/377492](https://doi.org/10.1086/377492)
- Zuckerman, B., Melis, C., Klein, B., Koester, D., & Jura, M. 2010, *ApJ*, 722, 725, doi: [10.1088/0004-637X/722/1/725](https://doi.org/10.1088/0004-637X/722/1/725)
- Zuckerman, B., & Young, E. D. 2018, in *Handbook of Exoplanets*, ed. H. J. Deeg & J. A. Belmonte (Cham: Springer International Publishing), 1545–1566, doi: [10.1007/978-3-319-55333-7\\_14](https://doi.org/10.1007/978-3-319-55333-7_14)